

4 Laminar Flame Dynamics

The flame dynamics of a laminar flat-flame burner were investigated. By starting with the simplest case possible; effects of turbulence, flame structure, and equivalence ratio fluctuations were eliminated. The laminar burner also allowed a platform to perform a proof-of-concept of the TDLAS system. The experimental frequency response functions of heat release rate to velocity perturbations were analyzed and compared to a 1-D numerical model. Analysis of experimental results yielded a compact model of the laminar flame transfer functions in terms of dimensionless magnitude and Strouhal number. The laminar flame study is described in this chapter.

4.1 Objectives

To accurately model flame dynamics, one must correctly describe an exceptionally complex system, including chemical kinetics, transport phenomena (heat transfer, mixing), and fluid mechanics. It would be foolish to attempt to develop models of real combustors without adequately understanding a simple system. By studying a flat (1-D) laminar flame, complications due to mixing and fluid mechanics can largely be eliminated. Knowledge can be built incrementally, moving to more complicated systems. Laminar flame dynamics also have direct application to devices that use laminar combustion, such as many furnaces and boilers.

The objective is to develop compact models of flame dynamics, based on important physical parameters that adequately describe the frequency response data. Models will be derived for reaction rate and acoustic forcing function dynamics.

4.2 Experimental Procedure

4.2.1 Measurement Process. A strict set of procedures was followed each time data was recorded to insure the repeatability and validity of the data. Before taking data, the burner was allowed a minimum of 30 minutes to reach steady-state at the desired operating conditions. All electronics were also operated a minimum of 15 minutes before recording data to allow any transients to decay. First, air was flowed through the system and mass-flow meters were turned on. Then, the fuel was turned on and the burner was lit. All remaining electronics, with the exception of the PMT power supply, were then switched on. The lights in the room were turned off, and the PMT power supply was switched on. Before opening the slit on the monochrometer, the current-to-voltage circuit was zeroed. The entrance slit was then opened to 15 microns, and the exit slit opened to 9 microns. It was then necessary to determine what voltage to apply to the speaker at each frequency. Due to the acoustics of the combustor, most notably a velocity node near 200 Hz, more voltage was applied at higher frequencies to achieve the correct velocity perturbation at the flame. To insure that the measured dynamics were in the linear range, the harmonics in the velocity signal were never allowed to be within 25 dB of the fundamental and no harmonics were observed in the OH* or temperature signals. The desired voltages were then entered into the Labview code used to run the experiments, `flame_dynamics.vi`. After the apparatus was allowed to reach steady state, the code was started and proceeded to force the speaker at each desired frequency, wait 45 seconds to allow transients to decay, then record data.

4.2.2 Frequency Response Data Analysis. The data acquisition system records time traces of signals. The data is then digitally filtered, scaled, and a spectral analysis is performed to obtain frequency response functions.

After the flame and electronics are given time to reach steady state, the data acquisition procedure is started. First, the current to the diode lasers is modulated so that a reference spectral absorption coefficient can be calculated using wavelength scanning (see Appendix B2). Then, the speaker is set to the desired frequency and amplitude. After allowing 45 seconds for the combustion process to reach steady-state, the system acquires time traces of velocity, diode laser intensities, pressure, intensity and reference intensity of the IR Helium-Neon laser, the OH* chemiluminescence, and a thermocouple

in the post-flame region. The speaker is then updated with the next desired frequency and amplitude, and the process is repeated. After data has been acquired for the range of frequencies, the current to the diodes is again modulated to take a reference spectral absorption coefficient.

The data analysis process starts by averaging the data for the reference diode laser intensities and calculates the spectral absorption coefficient. Then, for each frequency, the data is sent through a digital filter to remove unwanted frequency content. Care was taken to insure the digital filter has no effect on the phase of the measurement, as seen in Figure 4.1. The digital filter is especially needed for the diode laser intensities that experience low-frequency modulation due to flow discontinuities in the flame. The diode laser data is used to calculate temperature. The equivalence ratio is calculated from IR He-Ne intensities. A spectral analysis is then performed to calculate the frequency response between the output signal and input, either velocity or equivalence ratio.

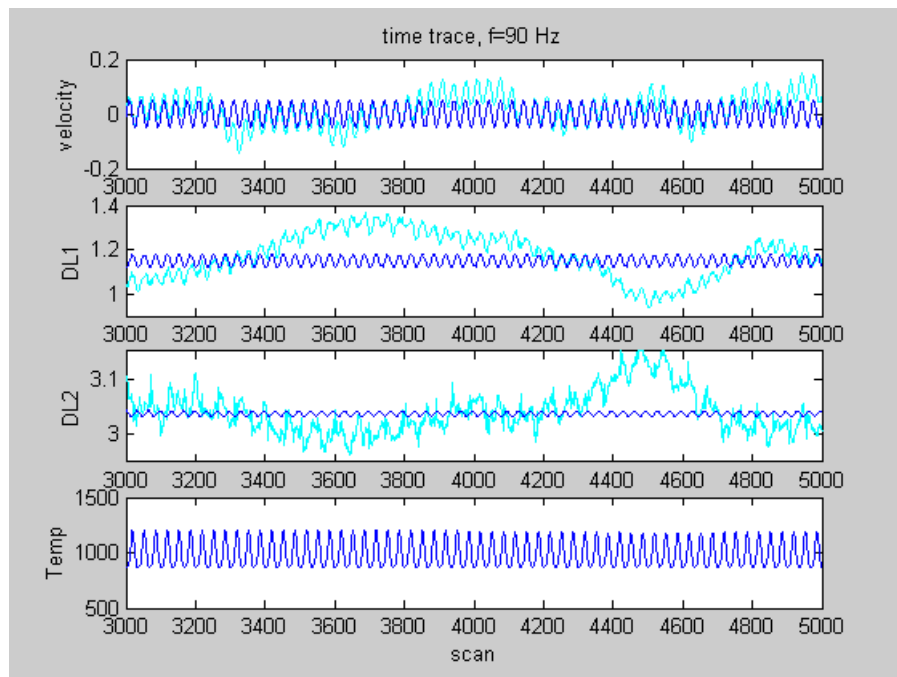
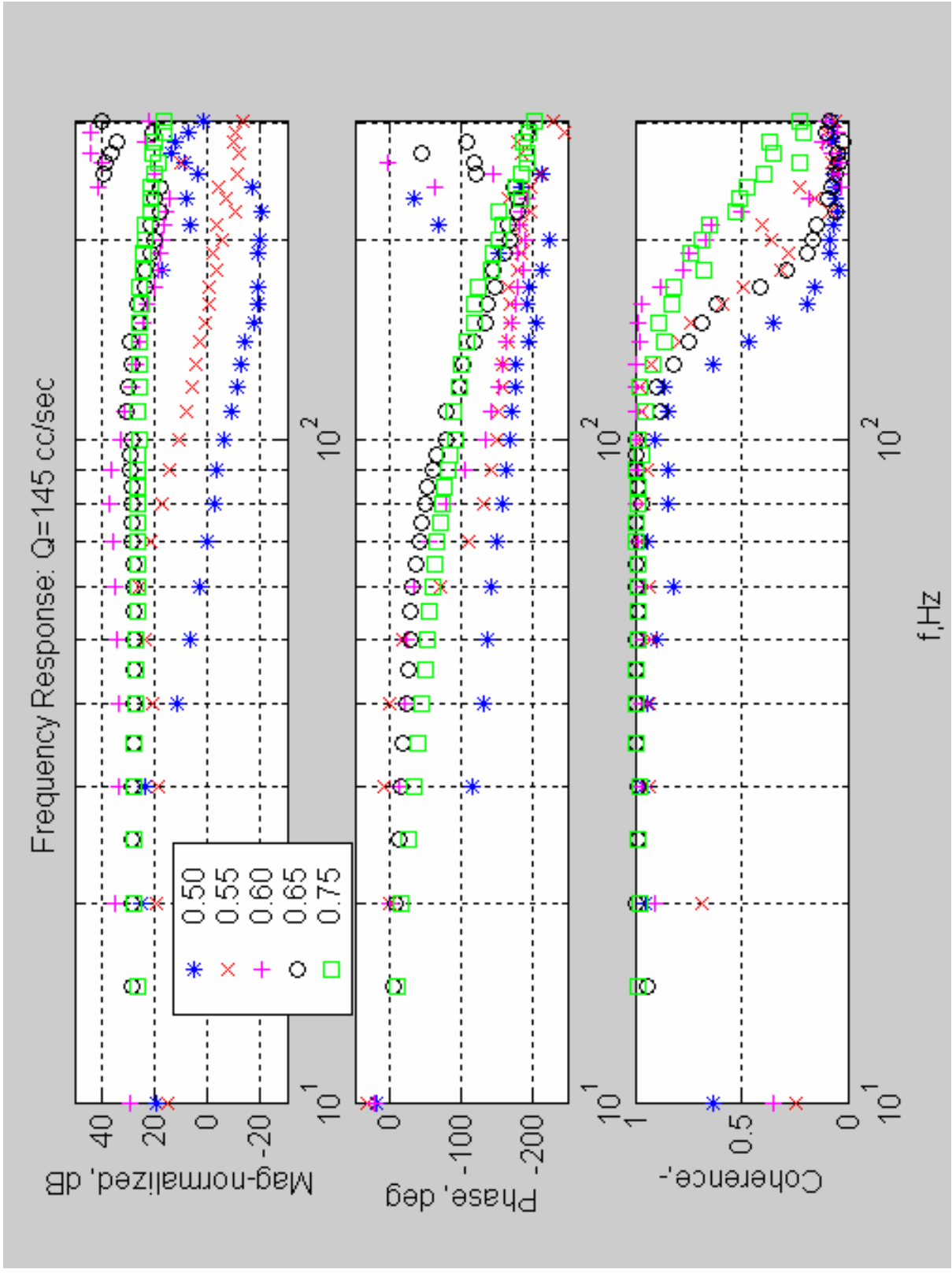


Figure 4.1. Time-Trace Data. The filtered signal (dark blue) maintains phase integrity with the raw signal (light blue).

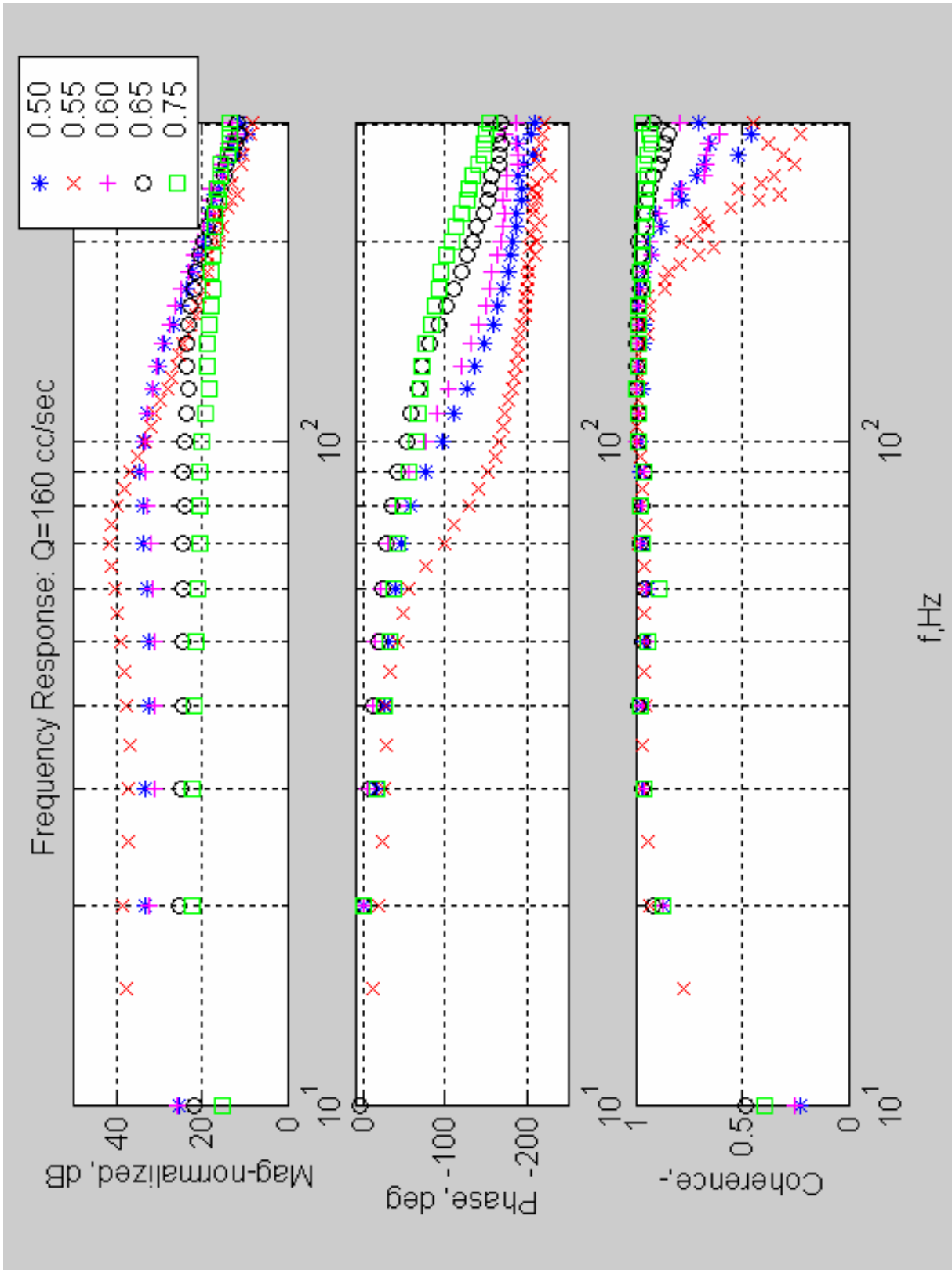
4.3 Experimental Results

Frequency response functions of flame dynamics were measured. OH* chemiluminescence was used as an indicator of chemical heat release rate, or reaction rate. Product gas temperature, measured via TDLAS, indicates the acoustic forcing function. Frequency response functions were recorded at flow rates of 145, 160, 180, and 200 cc/sec at equivalence ratios of 0.50, 0.55, 0.60, 0.65, and 0.75 for methane; and at flow rates of 145 and 200 cc/sec and equivalence ratios of 0.55 and 0.75 for ethane and propane.

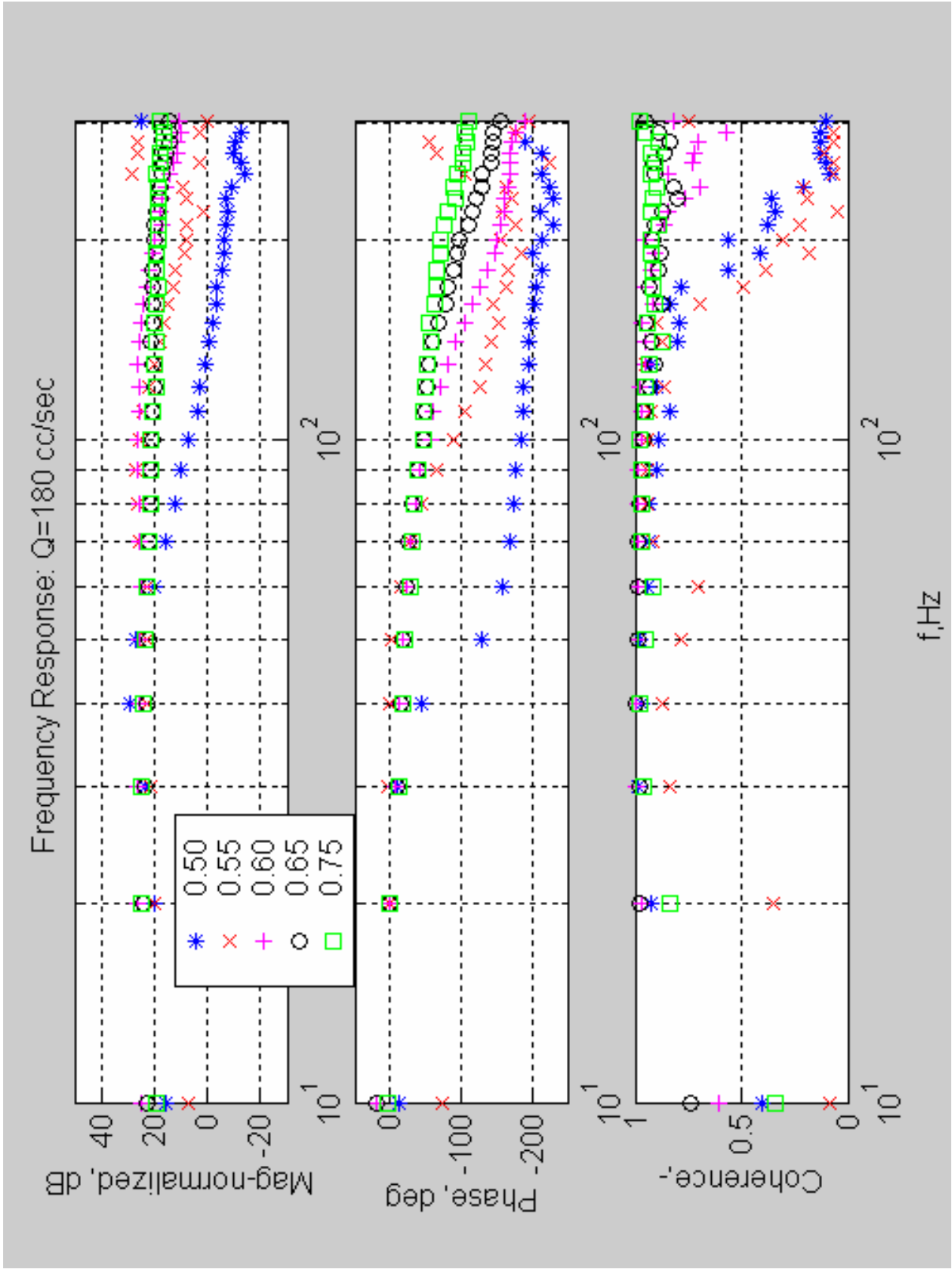
4.3.1. OH* Chemiluminescence Frequency Response Functions. The OH* chemiluminescence frequency response functions are an indicator of reaction rate dynamics. Results for methane are shown in Figure 4.2. Ethane results are shown in Figure 4.3, and propane results are shown in Figure 4.4. The bandwidth of reaction rate dynamics is approximately 250 Hz, as indicated by the coherence falling steeply. One dominant resonance is observed at frequencies between 50 and 150 Hz. This resonance increases in frequency with equivalence ratio and flow rate. The damping also increases with equivalence ratio and flow rate. A resonance indicates a complex-conjugate pair of poles, and thus 180 degrees of phase drop. However, the phase continues to drop after 180 degrees, suggesting a damped resonance at higher frequencies or time lag. The frequency response functions suggest the reaction rate dynamics can be adequately modeled by a second order system, i.e. two poles in the characteristic equation.



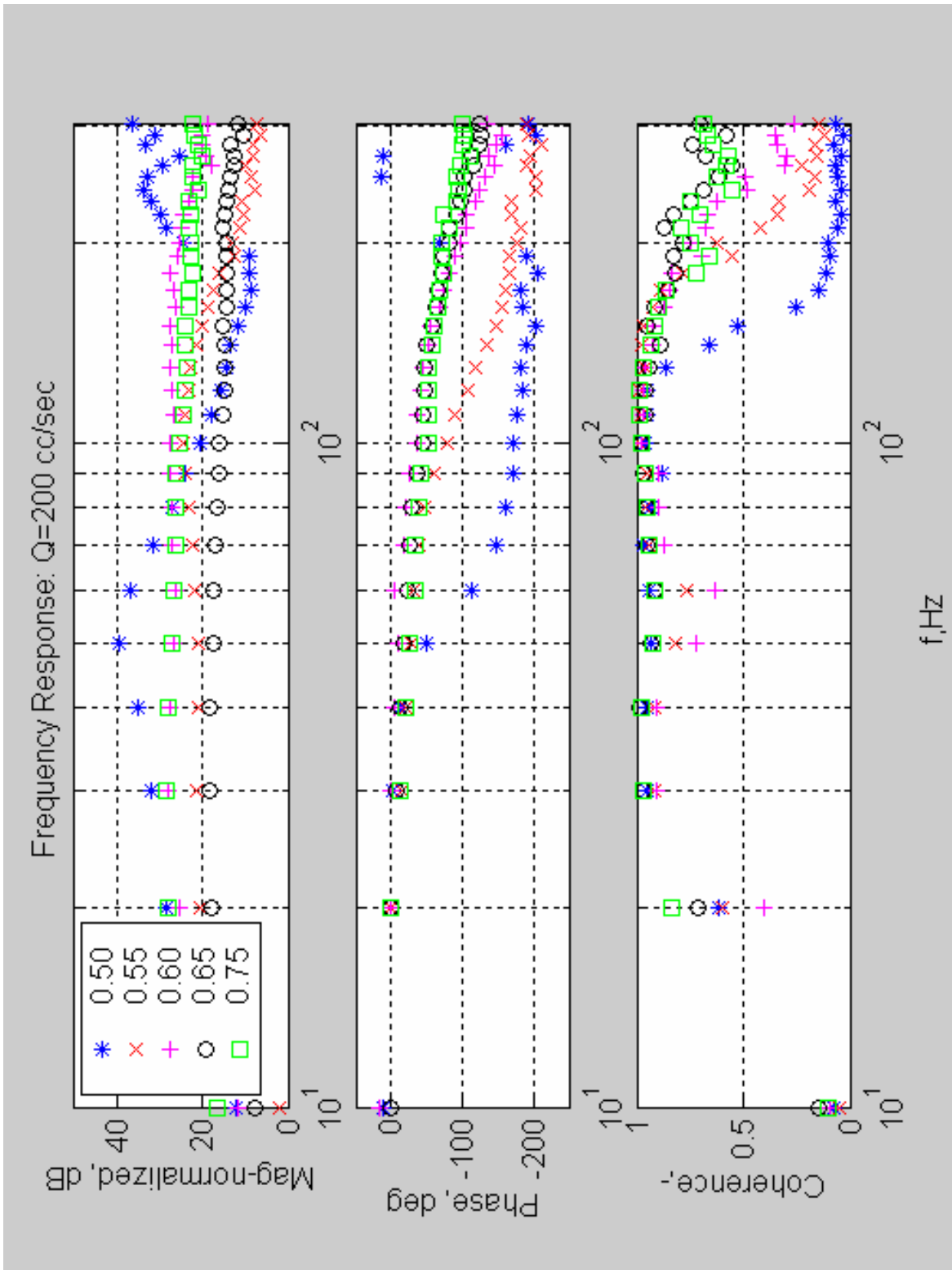
(a)



(b)

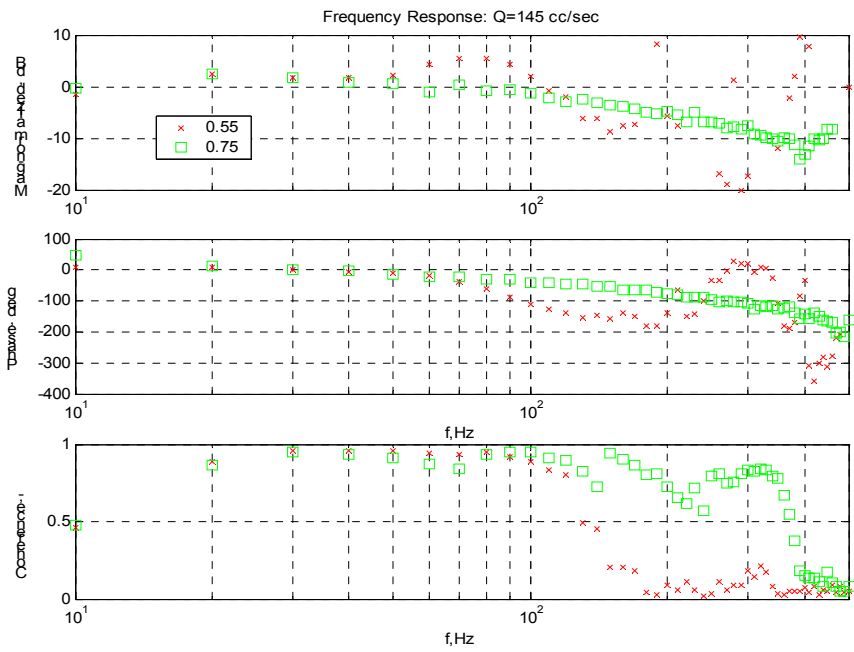


(c)

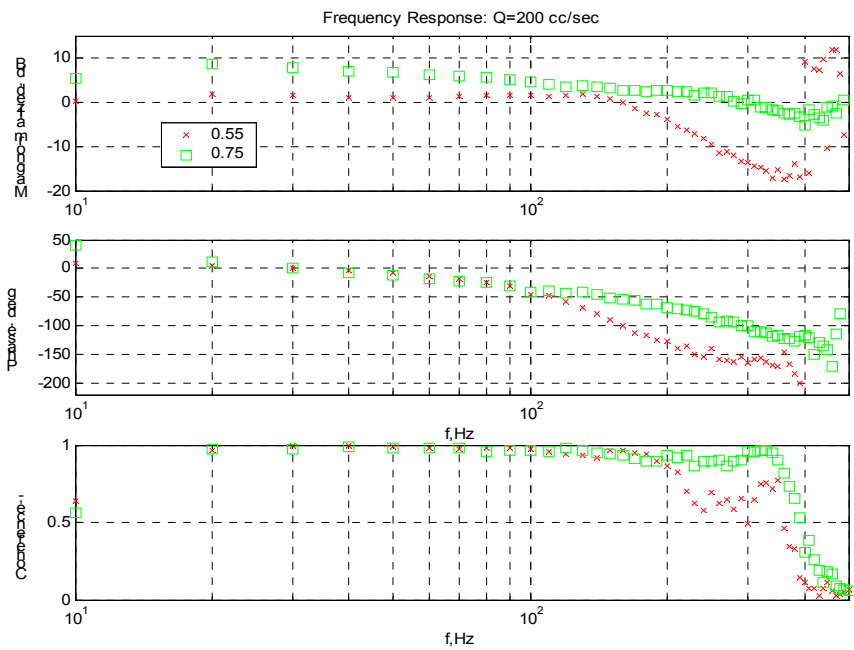


(d)

Figure 4.2. OH* Chemiluminescence Frequency Response - Methane. Normalized to DC value (a)Q=145 cc/sec, (b) Q=160 cc/sec, (c)Q=180 cc/sec, (d) Q=200 cc/sec

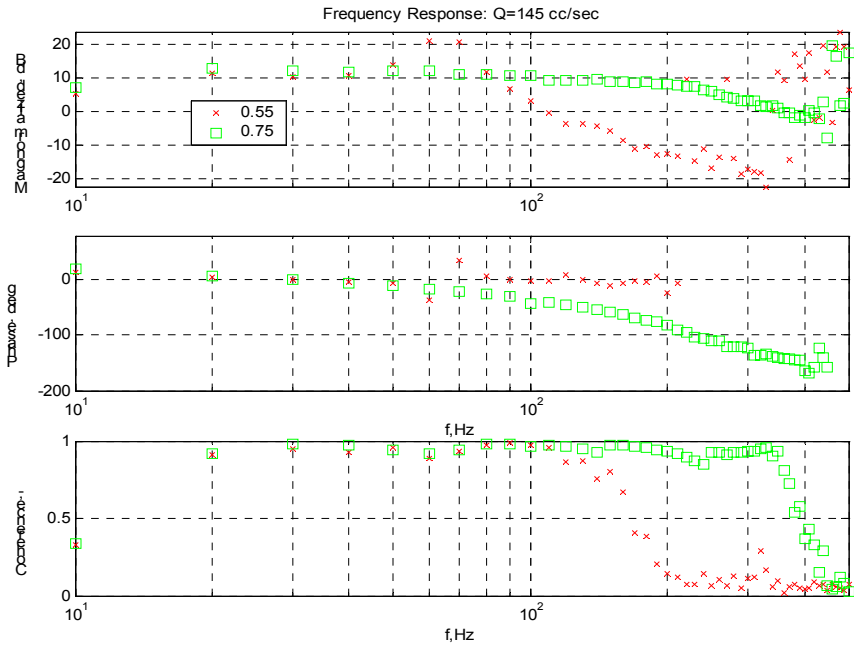


(a) Q=145 cc/sec

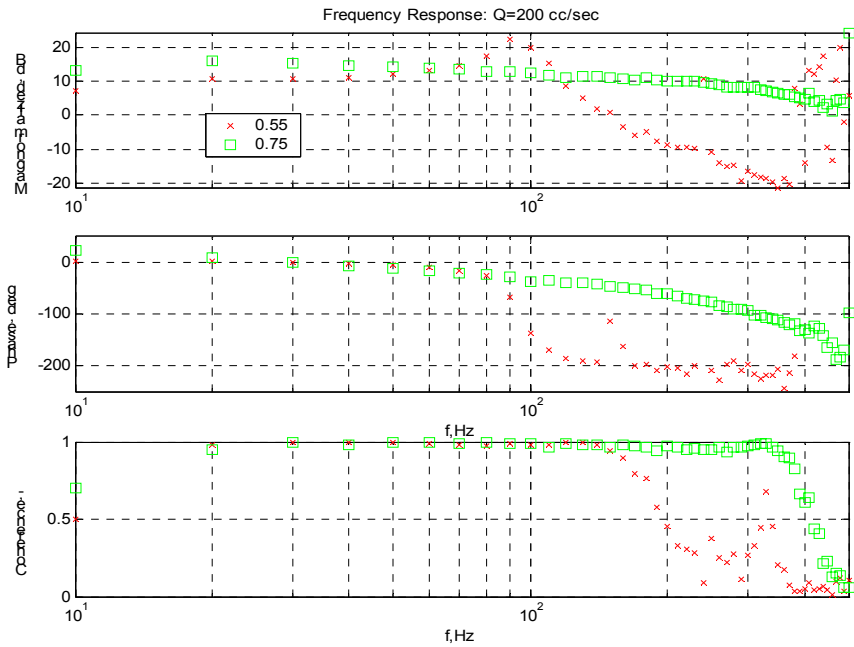


(b) Q=200 cc/sec

Figure 4.3. OH* Chemiluminescence Frequency Response - Ethane. Normalized to DC value (a)Q=145 cc/sec, (b) Q=200 cc/sec



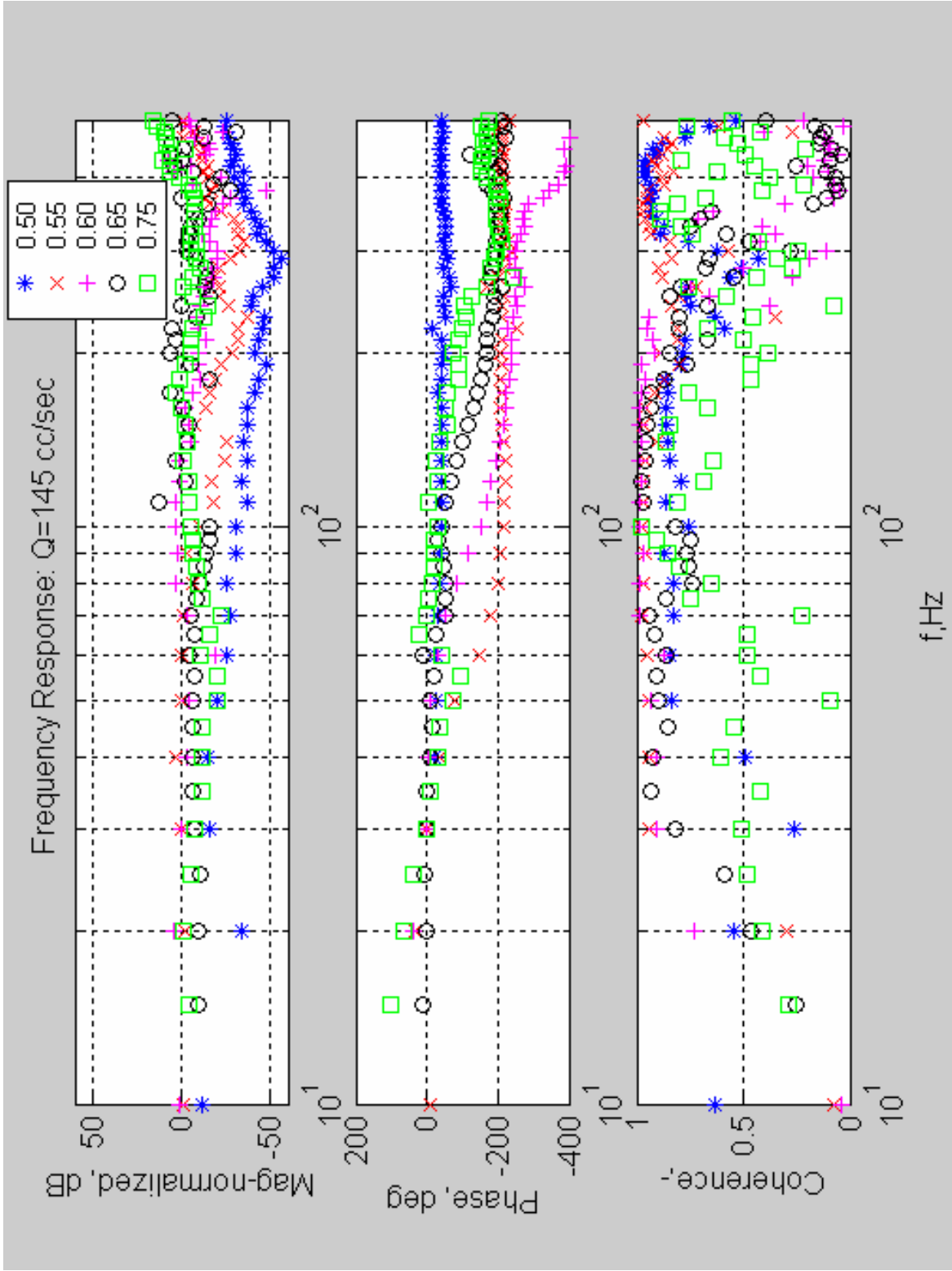
(a) Q=145 cc/sec



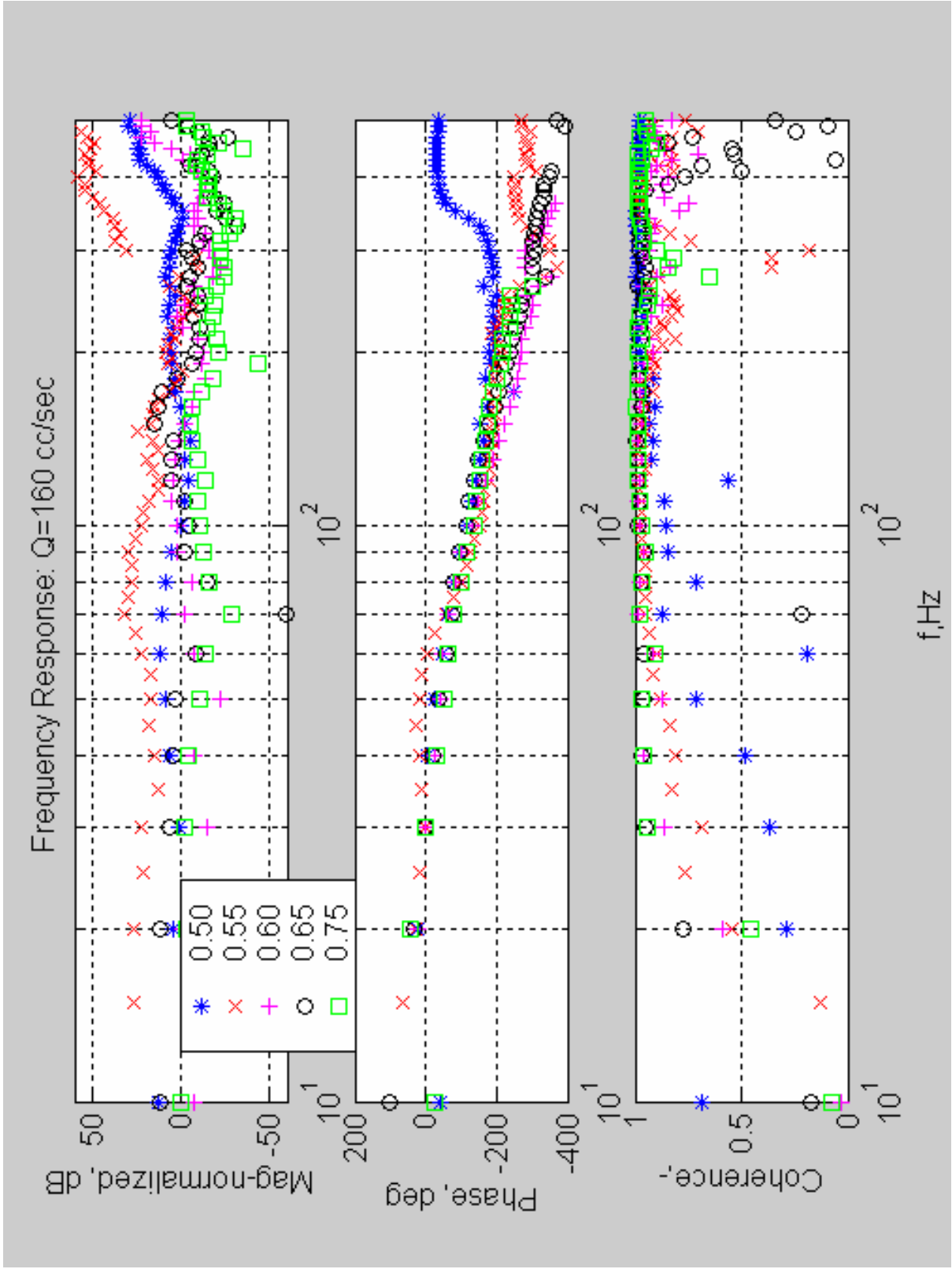
(b) Q=200 cc/sec

Figure 4.4. OH* Chemiluminescence Frequency Response - Propane. Normalized to DC value (a)Q=145 cc/sec, (b) Q=200 cc/sec.

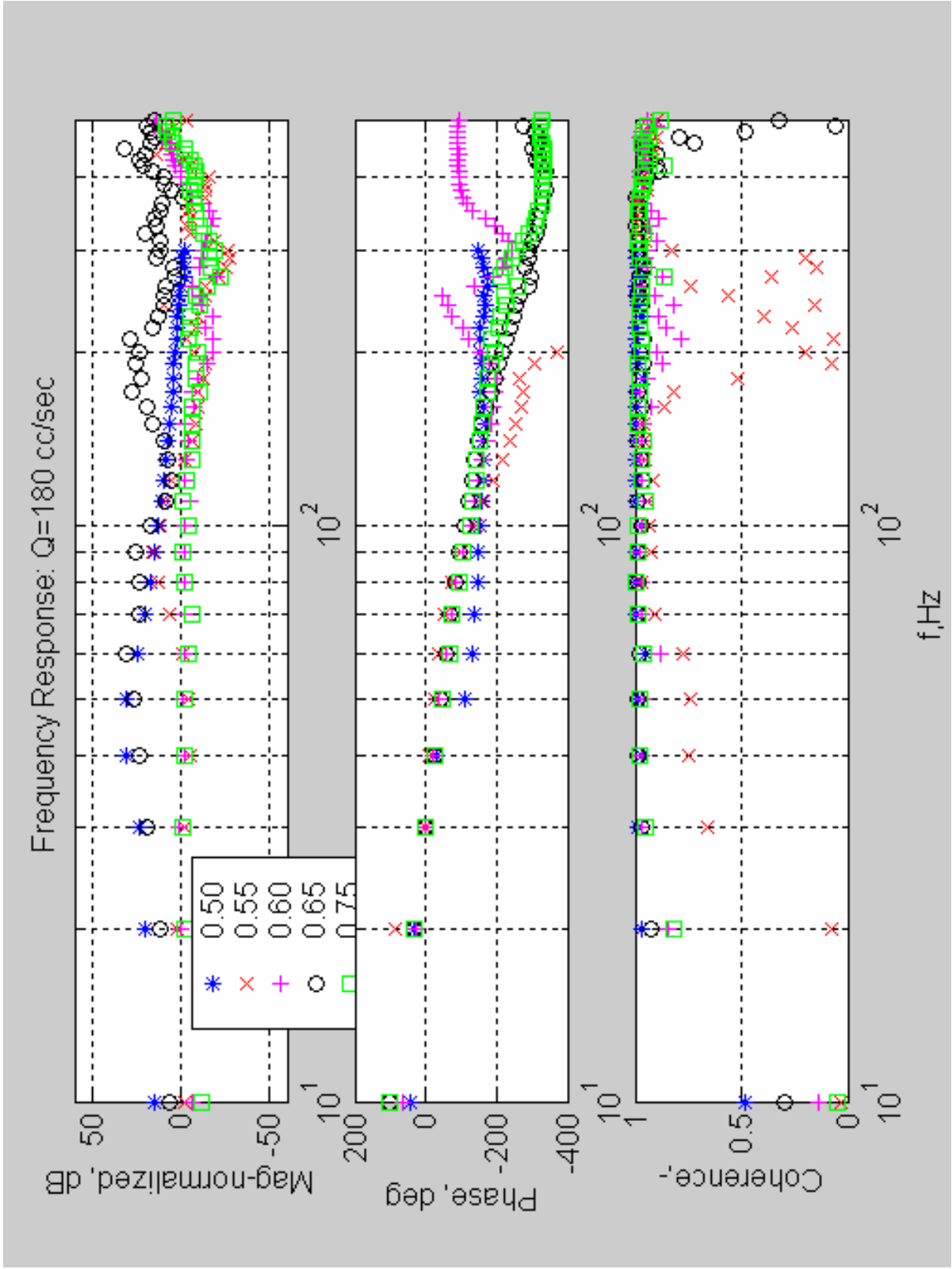
4.3.2. Temperature Frequency Response Functions. Parallel modeling efforts at the VACCG [1] indicate the acoustic forcing function is dominated by the time derivative of temperature, as discussed in chapter 1. Thus, a measurement of the temperature provides a good indicator of the effect of velocity perturbations on the enthalpy of the gases. Frequency response functions of product gas temperature for methane, ethane, and propane flames are shown in Figures 4.5, 4.6, and 4.7. The resonances follow the same trend as the reaction rate dynamics, increasing in frequency and damping with equivalence ratio and flow rate. Further observations of the temperature frequency response functions are discussed in the subsequent sections.



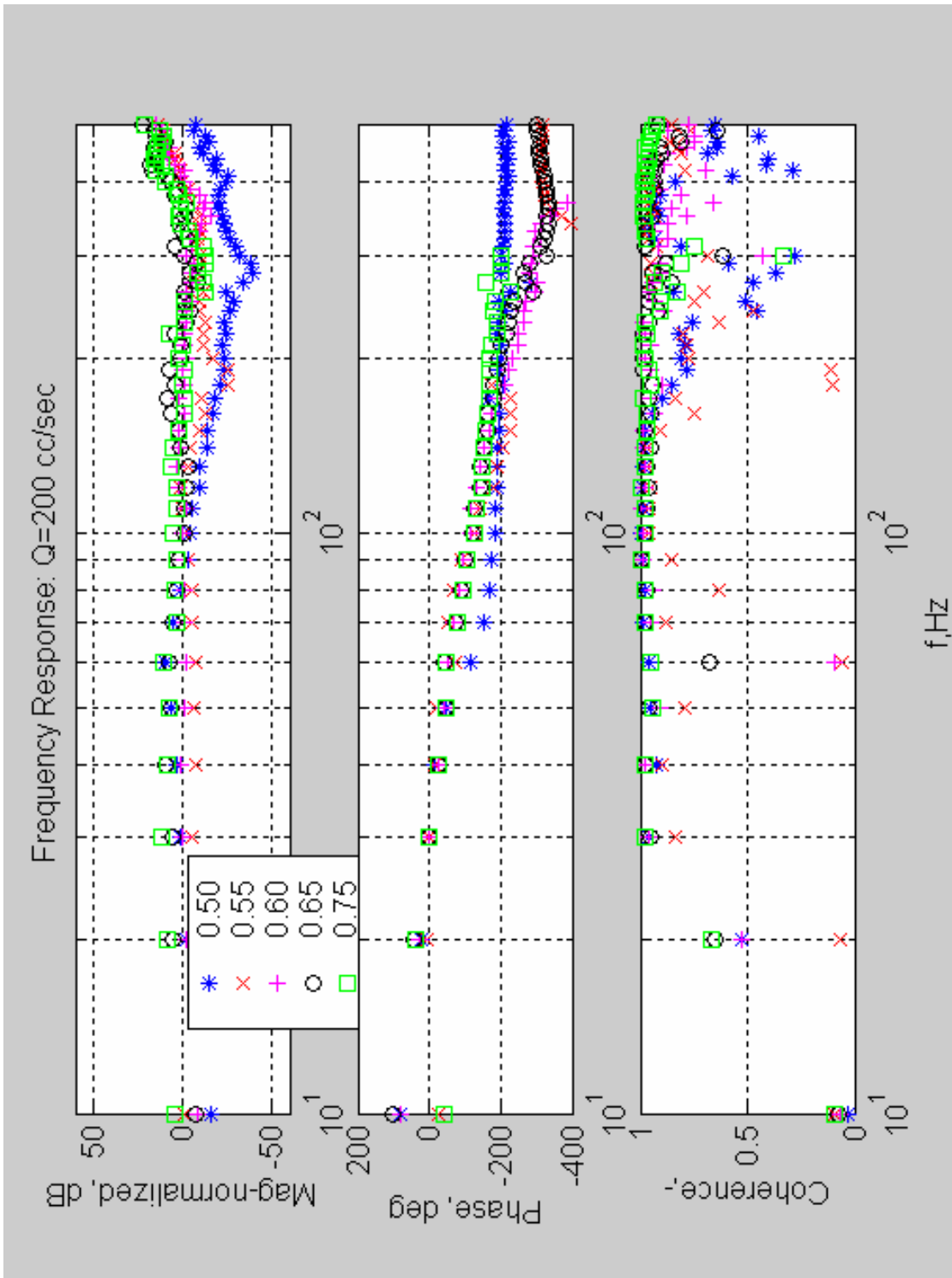
(a)



(b)

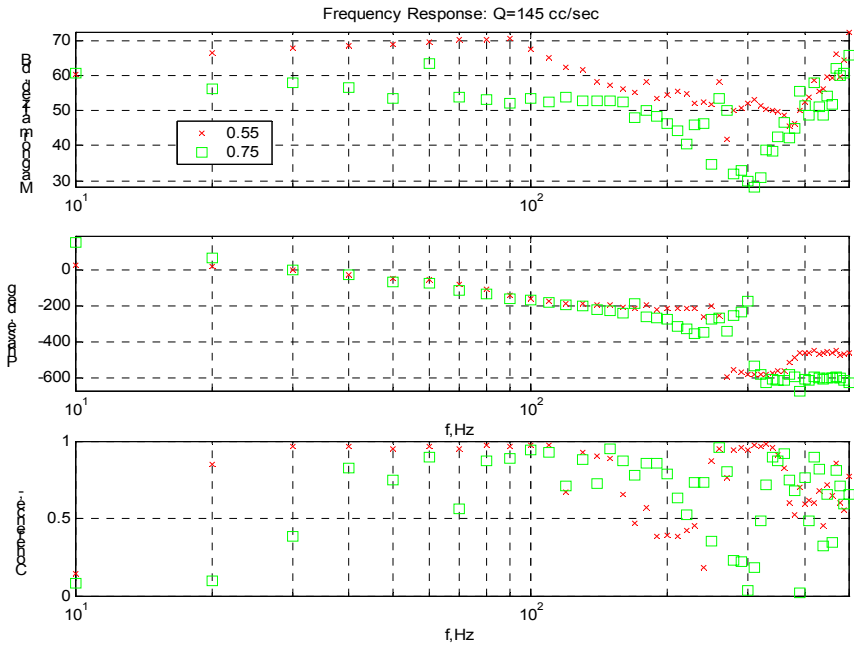


(c)

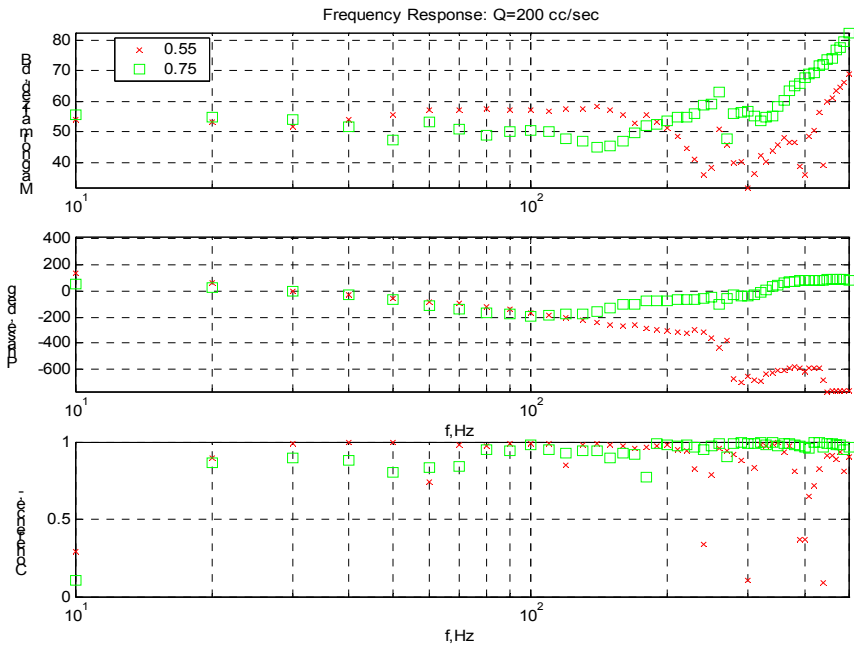


(d)

Figure 4.5. Temperature Frequency Response - Methane. Normalized to DC value.
 (a)Q=145 cc/sec (b) Q=160 cc/sec, (c)Q=180 cc/sec (d) Q=200 cc/sec

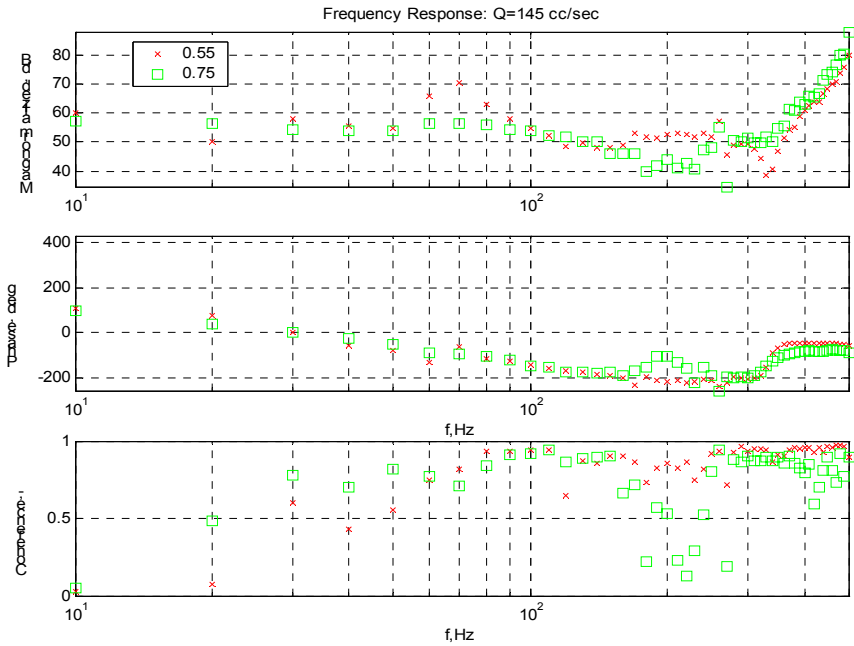


(a) Q=145 cc/sec

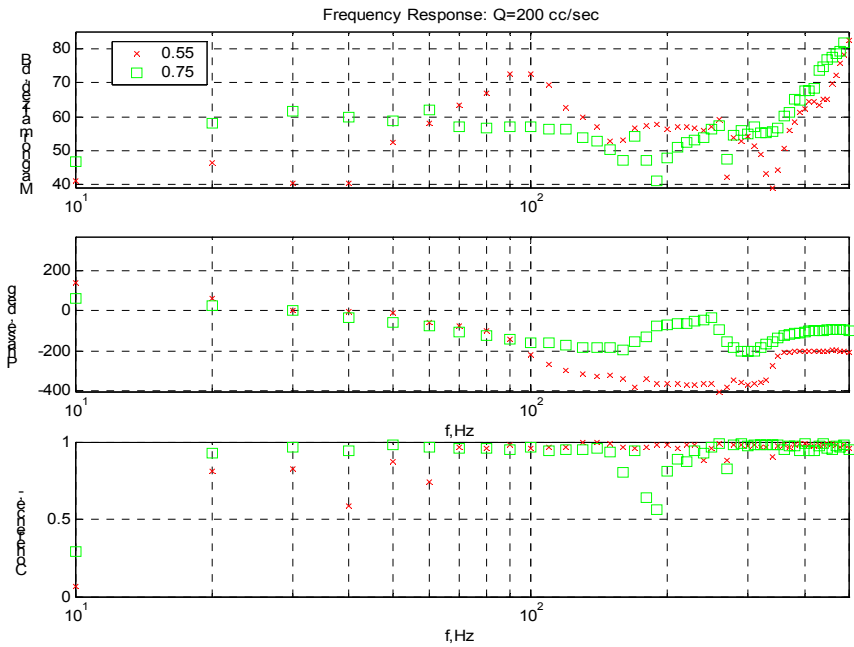


(b) Q=200 cc/sec

Figure 4.6. Temperature Frequency Response - Ethane. Normalized to DC value.
 (a) Q=145 cc/sec (b) Q=200 cc/sec



(a) Q=145 cc/sec



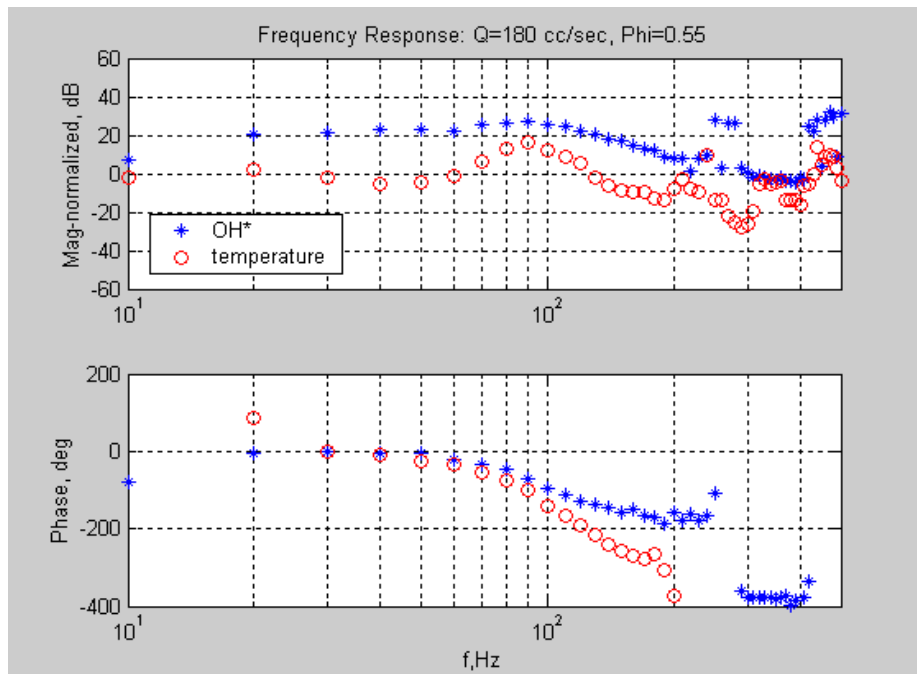
(b) Q=180 cc/sec

Figure 4.7. Temperature Frequency Response - Propane. Normalized to DC value.
 (a) Q=145 cc/sec (b) Q=200 cc/sec

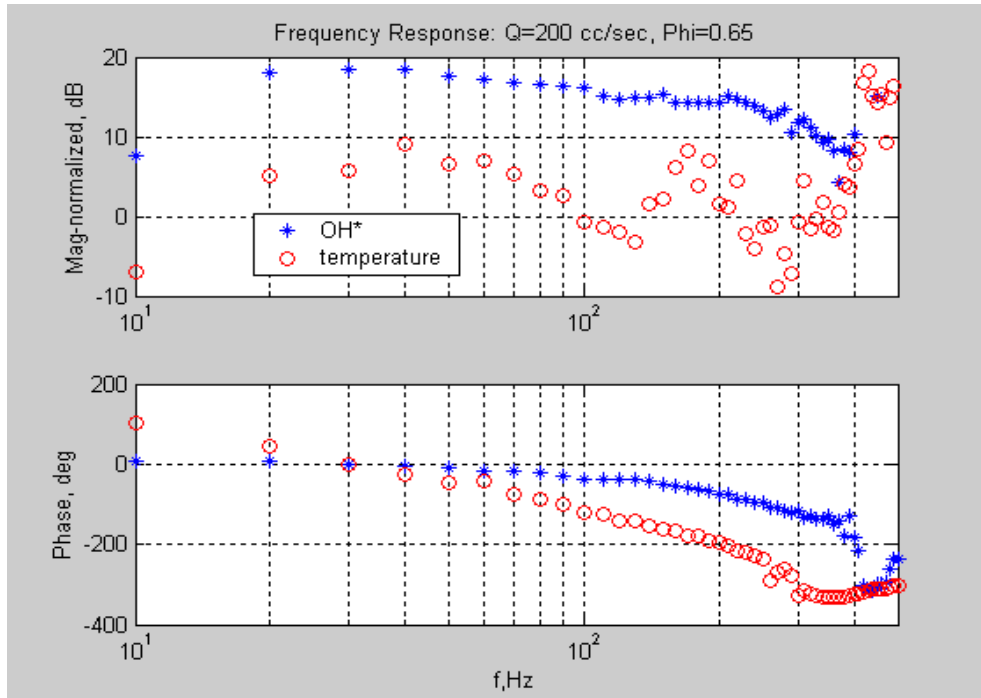
4.3.3 Comparison of Reaction Rate and Acoustic Forcing Function Dynamics.

Although primary resonances in reaction rate and acoustic forcing function behave similarly with flow rate and equivalence ratio, the damping ratio is considerably different. As seen in Figure 4.8, the dominant resonances in reaction rate and acoustic forcing function occur at approximately the same frequencies. However, acoustic forcing function resonances are much more lightly-damped, as evidenced by the steeper phase drop and sharper peaks in magnitude. The reaction rate dynamics have a bandwidth of approximately 250 Hz, while the acoustic forcing function continues to respond coherently beyond 1 kHz. This suggests that, in the laminar flame, reaction rate governs the acoustic forcing function at frequencies below 200 Hz. Above 200 Hz, acoustic forcing function dynamics are governed by heat transfer. It is probable that convection dominates at these frequencies, due to the bandwidth and transparent nature of the gases.

Vital to this discussion is that RR is not dynamically equivalent to the acoustic forcing function. Flame models and control algorithms cannot, therefore, be based on chemiluminescence without taking these differences into account.



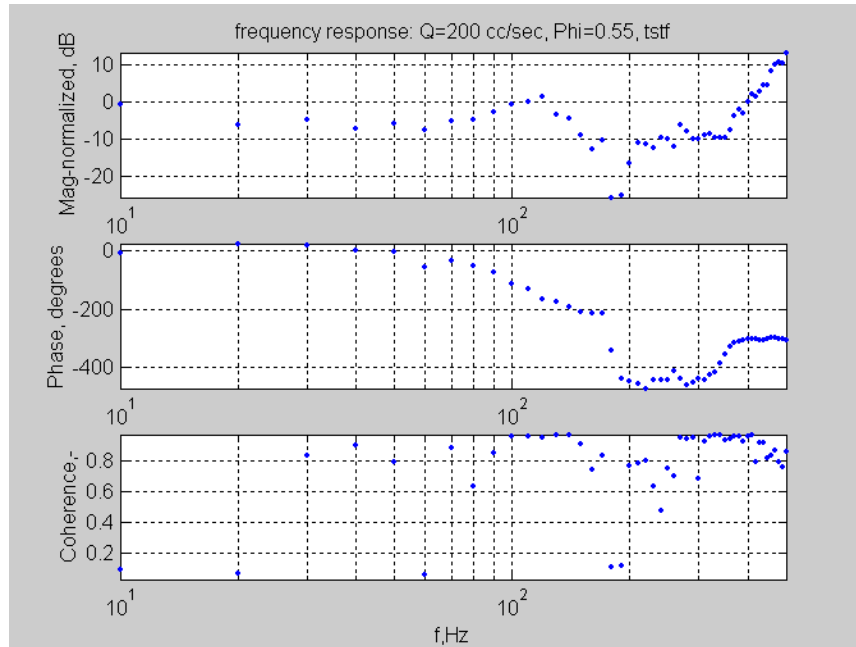
(a) $Q=180$ cc/sec, $\Phi=0.55$, Methane



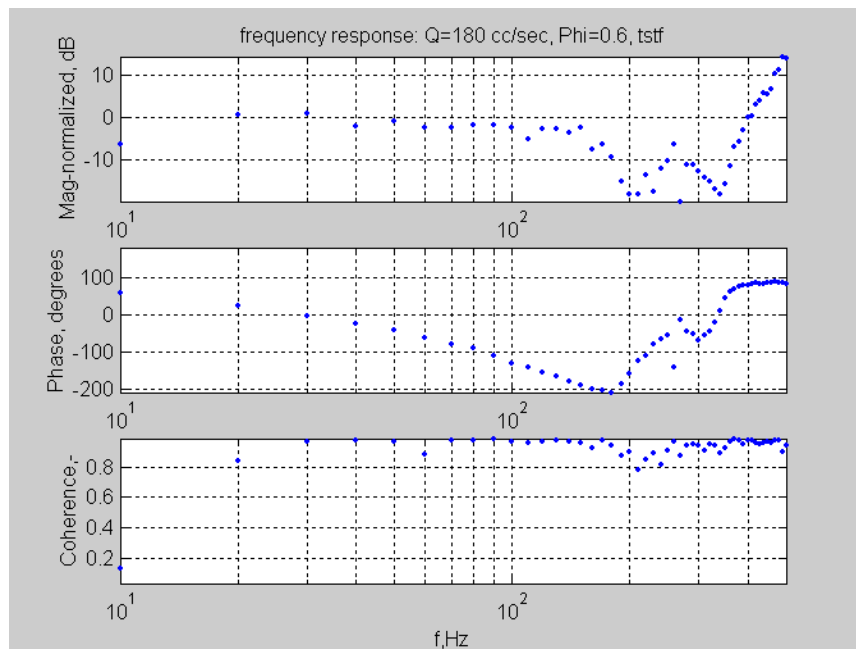
(b) $Q=200$ cc/sec, $\Phi=0.65$, Methane

Figure 4.8. Comparison of Reaction Rate and Acoustic Forcing Function Dynamics. The damping and bandwidth of the frequency responses are dissimilar.

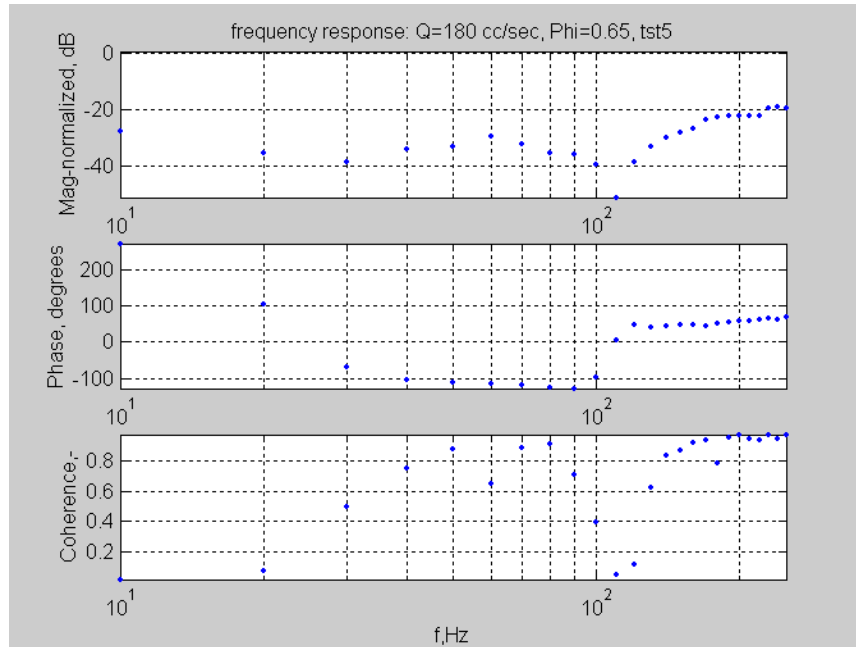
4.3.4 Zeros in Temperature Frequency Response Functions. Zeroes are observed in the AFF frequency response functions, as seen in Figure 4.9. Zeroes typically suggest wave cancellation, such as in acoustics. In this case, it is possible that entropy waves propagating off a wrinkled flame front result in zeroes [2]. Another possibility is that the zeroes correspond to symmetric flame front modes, where fluctuations would be integrated out. Schematics of these concepts are shown in Figure 4.10. Further evidence of a wrinkled flame front is discussed in the next section.



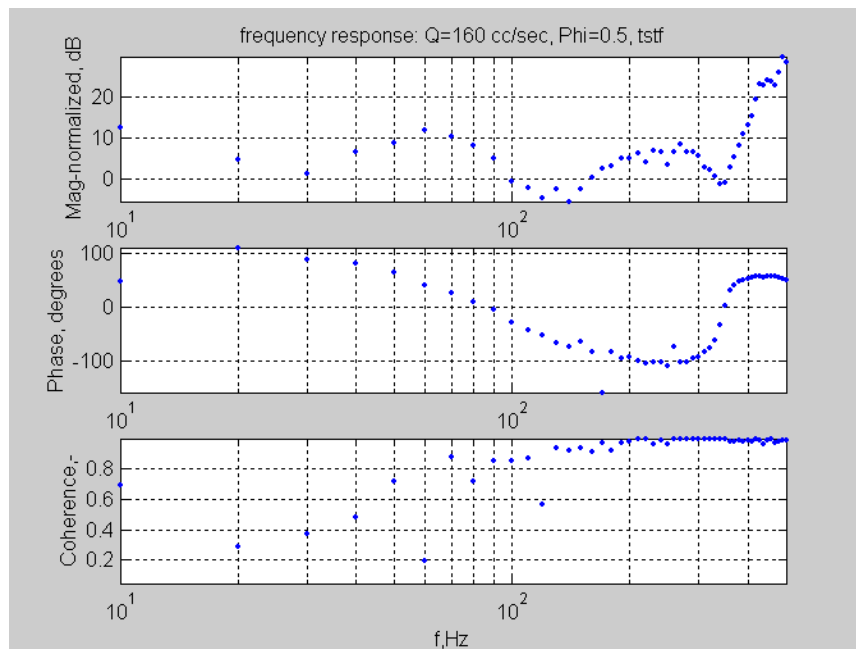
(a) Q=200 cc/sec, $\Phi=0.55$, Methane



(b) Q=180 cc/sec, $\Phi=0.60$, Methane



(c) Q=180 cc/sec, $\Phi=0.65$, Methane



(d) Q=160 cc/sec, $\Phi=0.50$, Methane

Figure 4.9. Zeros in the Temperature FRF's. A phase rise of 180 degrees and an inverted peak in the magnitude indicate a set of complex conjugate zeros.

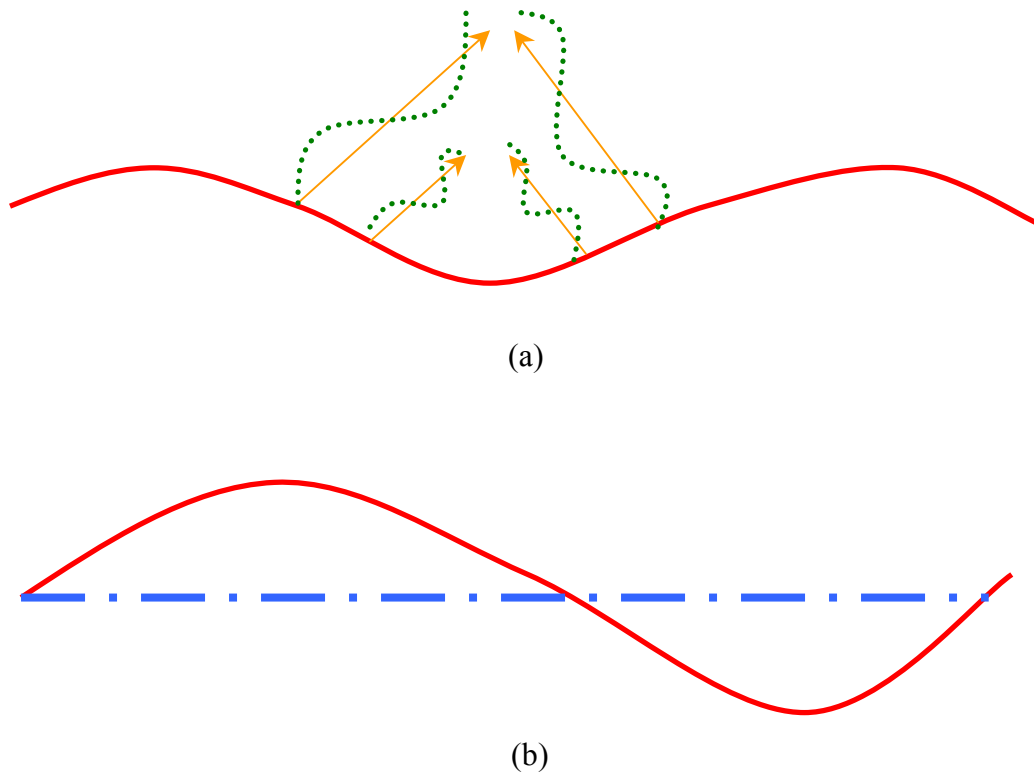


Figure 4.10. Possible Causes of Zeros. (a) entropy wave interaction, (b) symmetric modes.

4.3.5 Evidence of Flame Wrinkling. Many times in the acoustic forcing function frequency responses, a resonance is observed without the corresponding phase drop, as seen in Figure 4.3. It was proposed that these extraneous resonances are due to the 2-D effects along the path length. For flame dynamics, this corresponds to wrinkling of the flame front. Many researchers cite evidence of flame wrinkling, including theoretical [3-7], and experimental work [3, 4]. A picture of a wrinkled flame is shown in Figure 4.11.

The TDLAS measurement is a line-of-sight measurement. The arrangement used in this experiment resulted in the beam passing through the flame twice, as shown in Figure 3.5. Ideally, the measurement would integrate effects spatially on a plane downstream of the flame, assuming plane-wave acoustics. The line-of-sight measurement integrates effects along the path length, disabling it from providing spatial resolution.

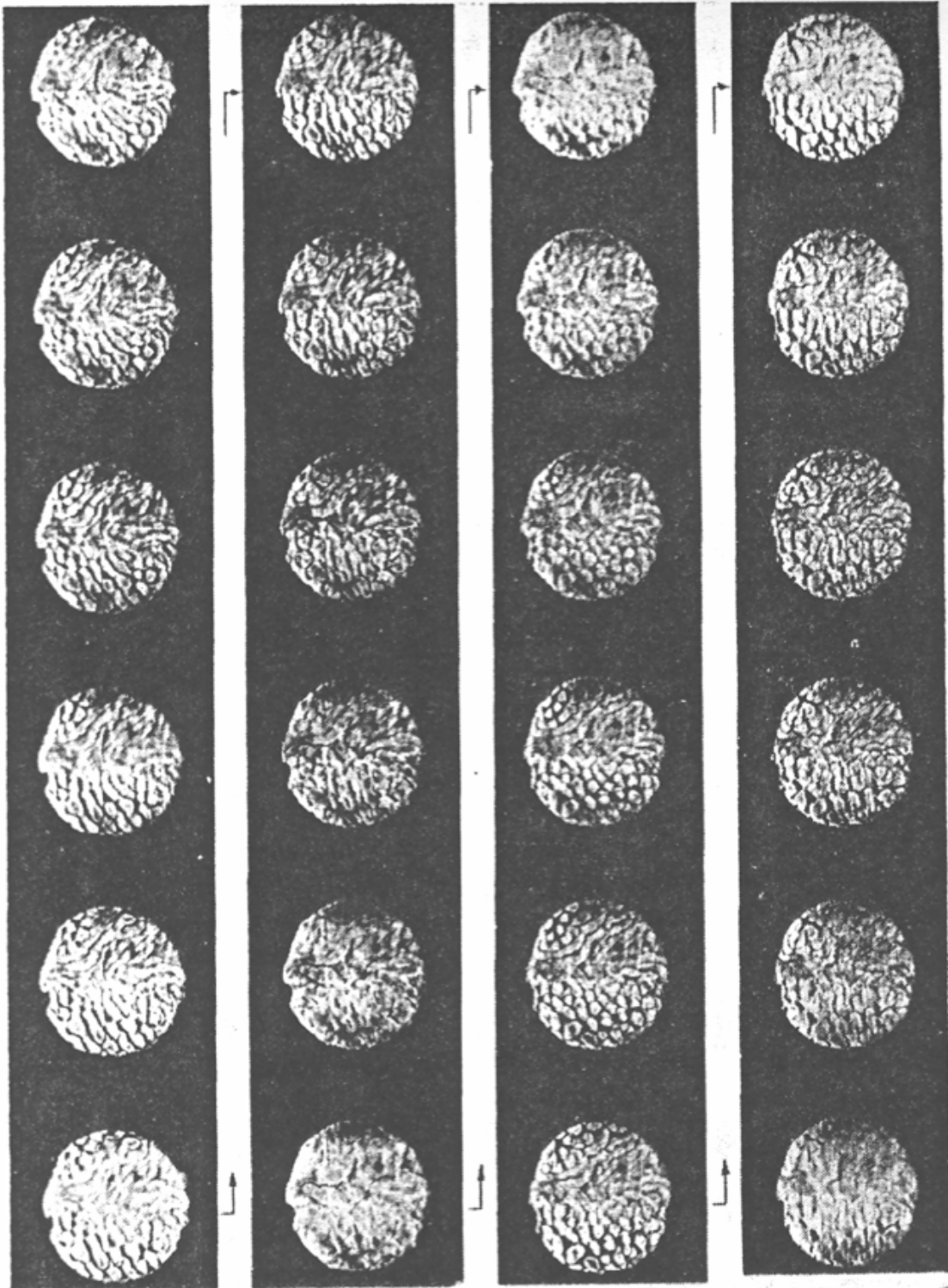


Figure 4.11. Wrinkled Flame Front. High-speed shadowgraph motion picture of vibration-induced cell structure at moderate vibration amplitude. Tube i.d. 10.0 cm, Approx. 1500 frames/sec. Image from [3].

To lend credence to this hypothesis, a line-of-sight measurement of a 2-D phenomenon was simulated. A schematic of the model coordinates are shown in Figure 4.12. The iso-surface (simulating the flame front) was constructed to fluctuate in time and space, as shown in Figure 4.13. At each point in time, the number of points on the iso-surface that fall in a specified y range was counted, generating a time-varying signal like that in Figure 4.14. A frequency response was taken at the frequency of the time fluctuation. A forced frequency response was generated by repeating these steps for a range of fluctuations in time, keeping the spatial fluctuation constant. The final result simulates a forced response of a line-of-sight measurement on a 2-D phenomenon. As seen in Figure 4.15, the simulation shows that resonances with no associated phase are produced. This is similar to the observations in the temperature frequency response functions.

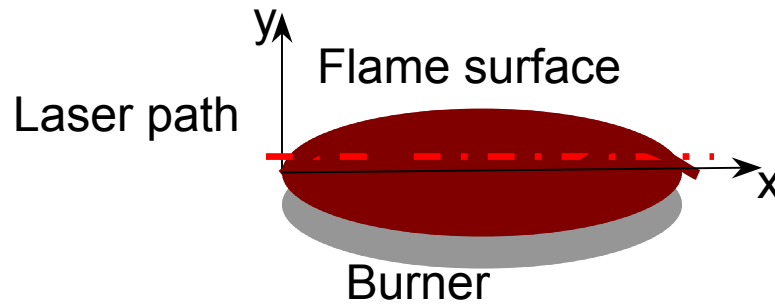


Figure 4.12. 2-D Model Coordinates. A line-of-sight measurement on a 2-D phenomenon.

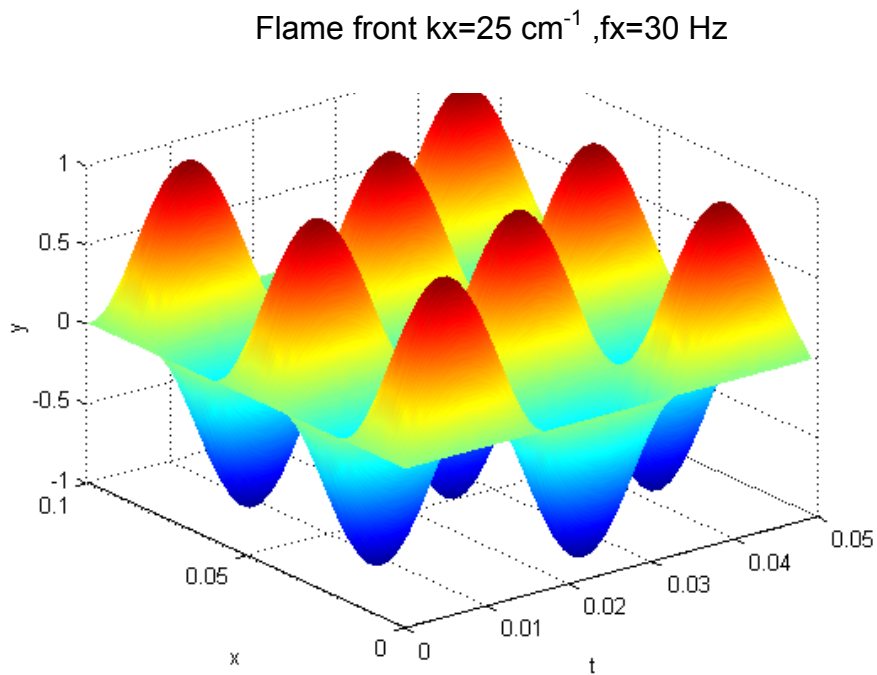


Figure 4.13. Iso-Surface. The surface represents a vertical plane of the flame front, fluctuating in time (t), and space (x).

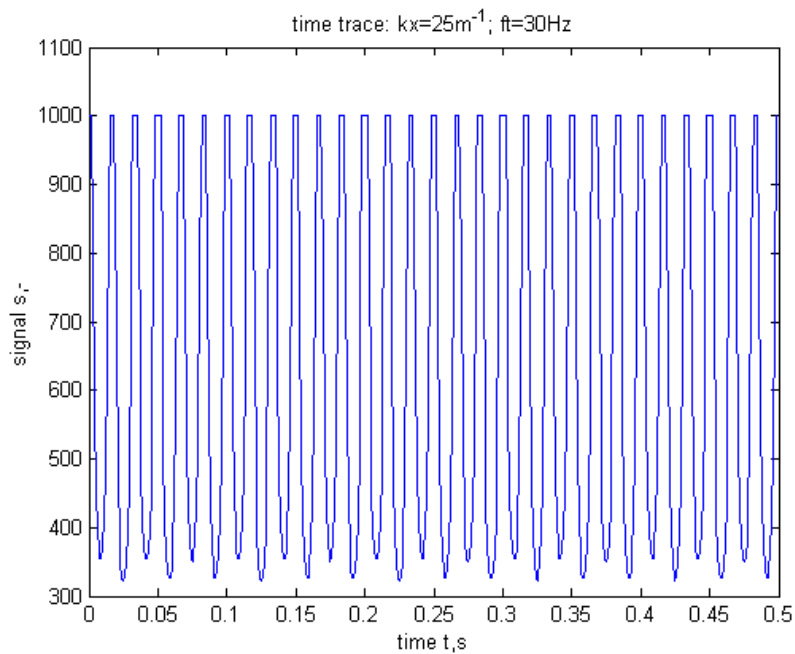


Figure 4.14. Simulated Signal. Integration over the y -range $[-0.4,0.6]$ generates a time-varying signal representing the line-of-sight measurement.

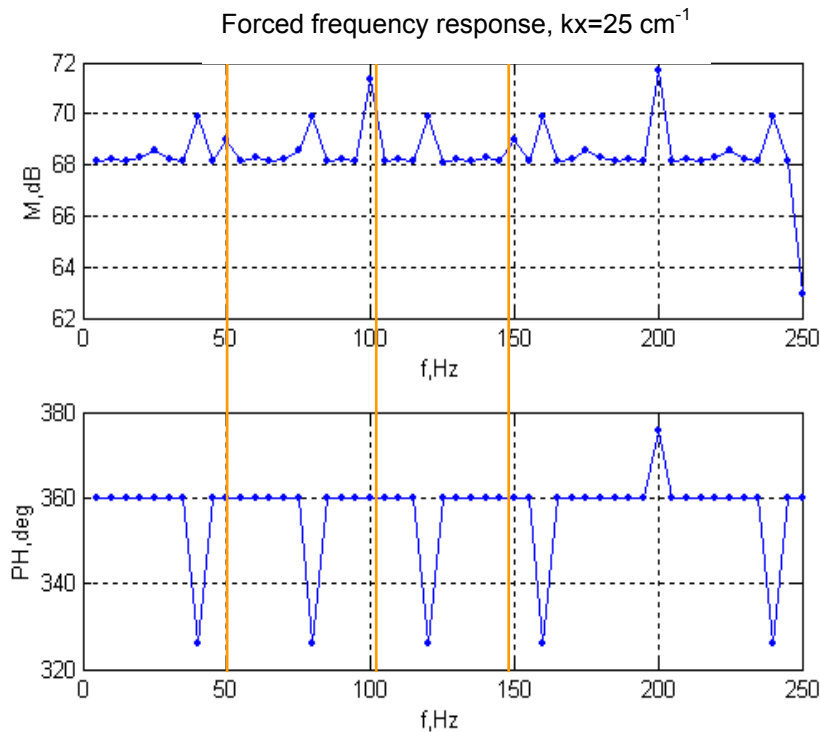
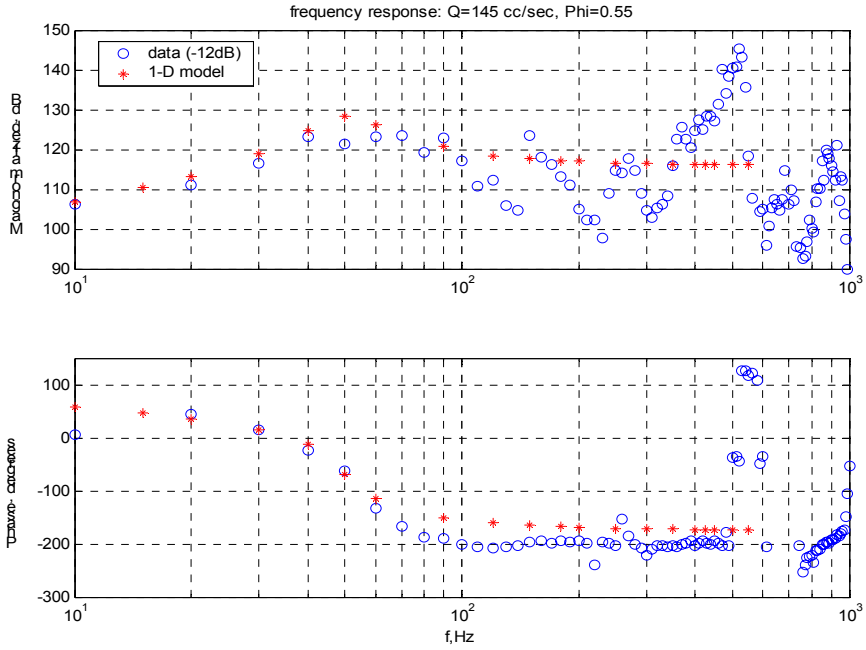
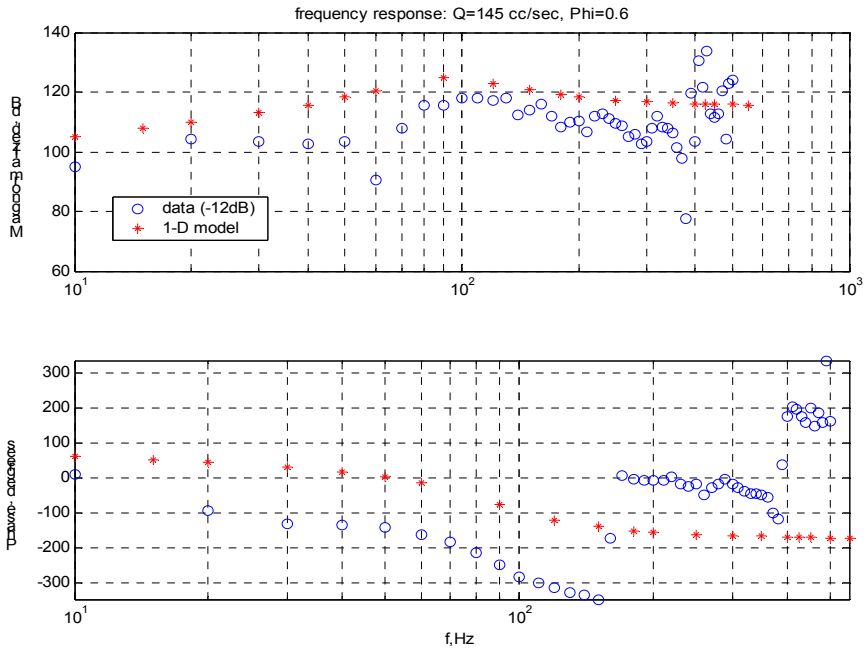


Figure 4.15. Forced Frequency Response. The FRF shows resonances with no phase drop.

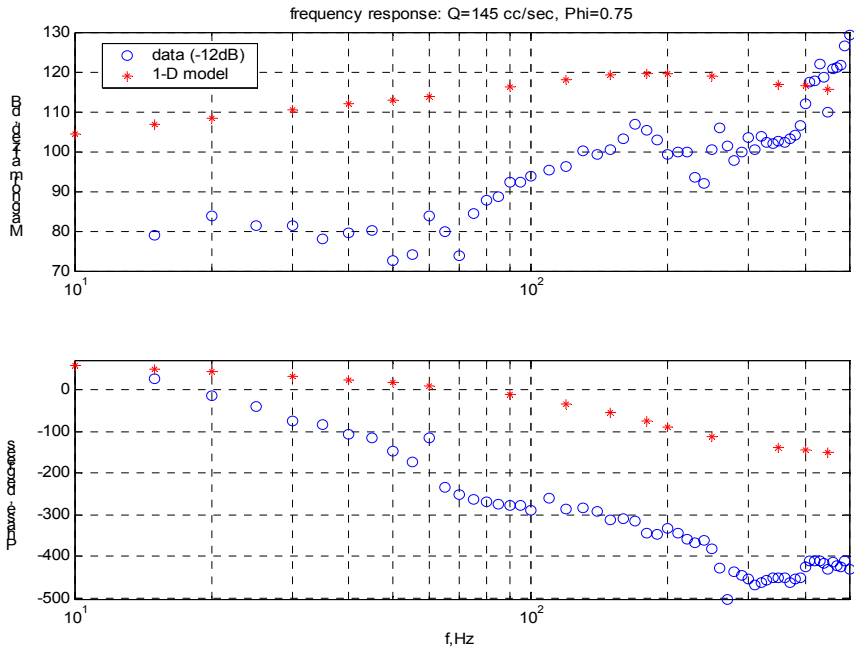
4.3.6 Comparison to Laminar Flame Code. Ludwig Haber and David Losh of the VACCG developed a dynamic model of a 1-D, burner-stabilized flame by modifying the PREMIX code from Sandia National Laboratory [8]. The model uses the full GRI-MECH chemistry model for methane [9] and includes radiative, convective, and conductive heat transfer. The model results closely match the experimental results of the acoustic forcing function frequency response functions, as seen in Figure 4.16. The measurement was a local (in axial space) measurement, while the model allows a prediction of the global frequency response of the acoustic forcing function. The results for several axial locations, as well as the global measurement, are compared in Figure 4.17.



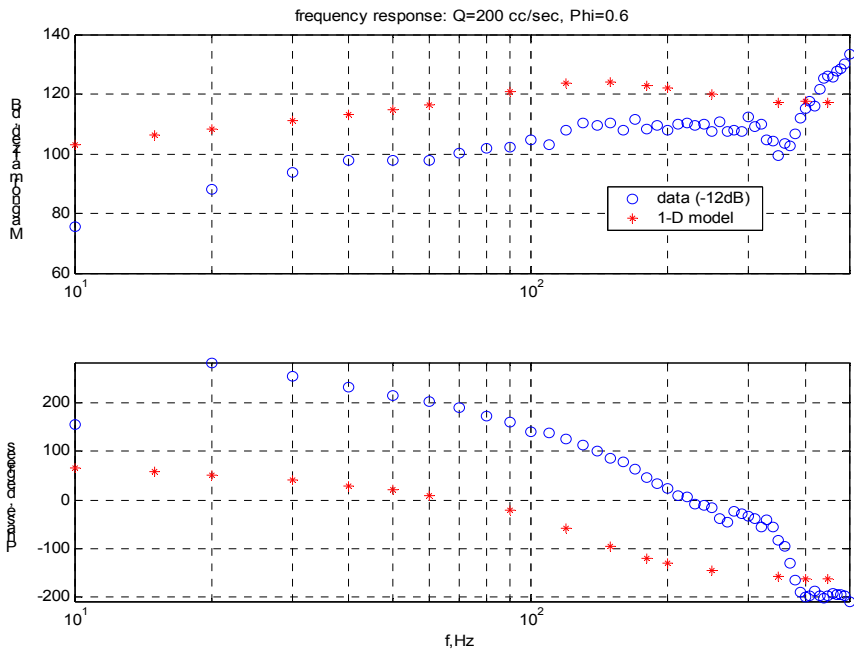
(a) Q=145 cc/sec, $\Phi=0.55$



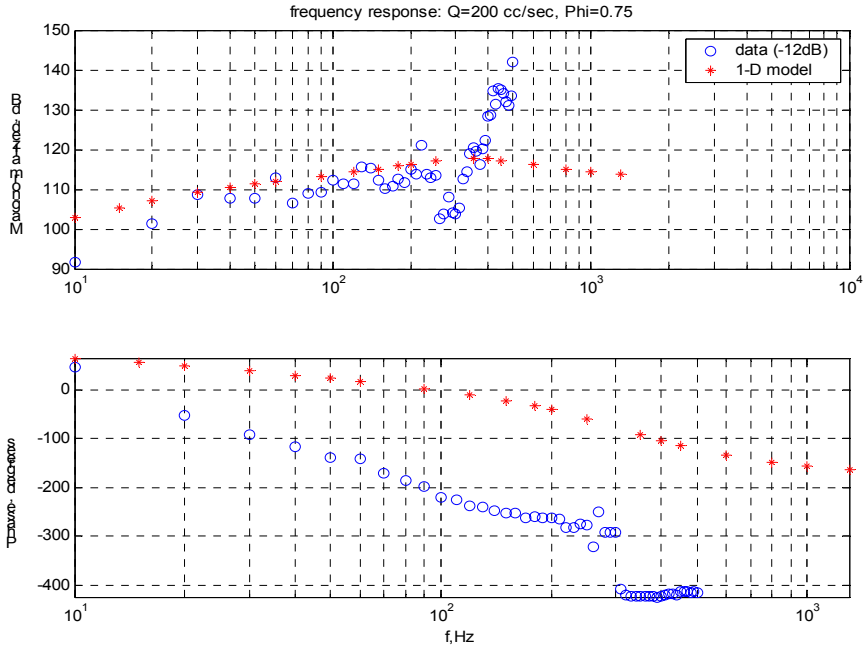
(b) Q=145 cc/sec, $\Phi=0.60$



(c) Q=145 cc/sec, $\Phi=0.75$

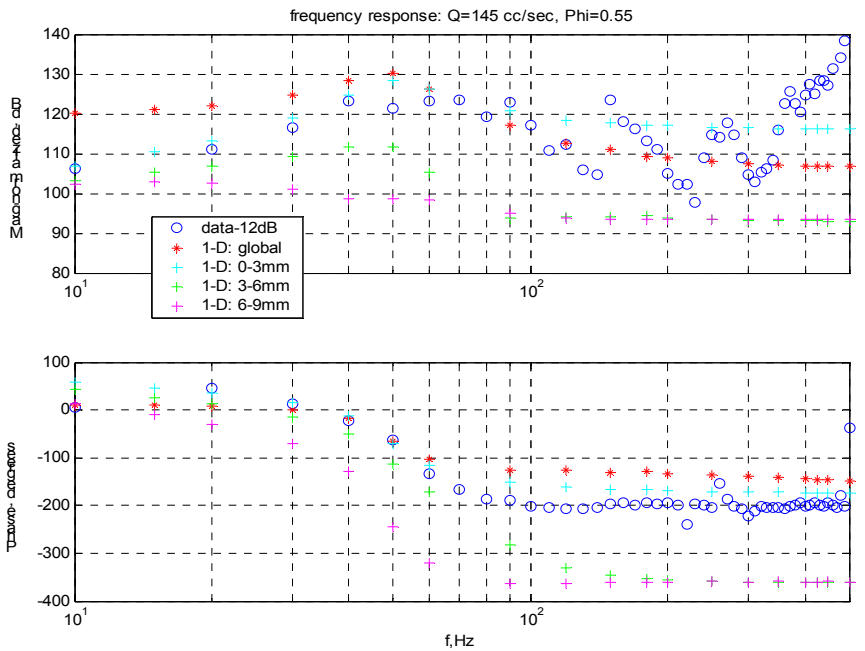


(d) Q=200 cc/sec, $\Phi=0.60$

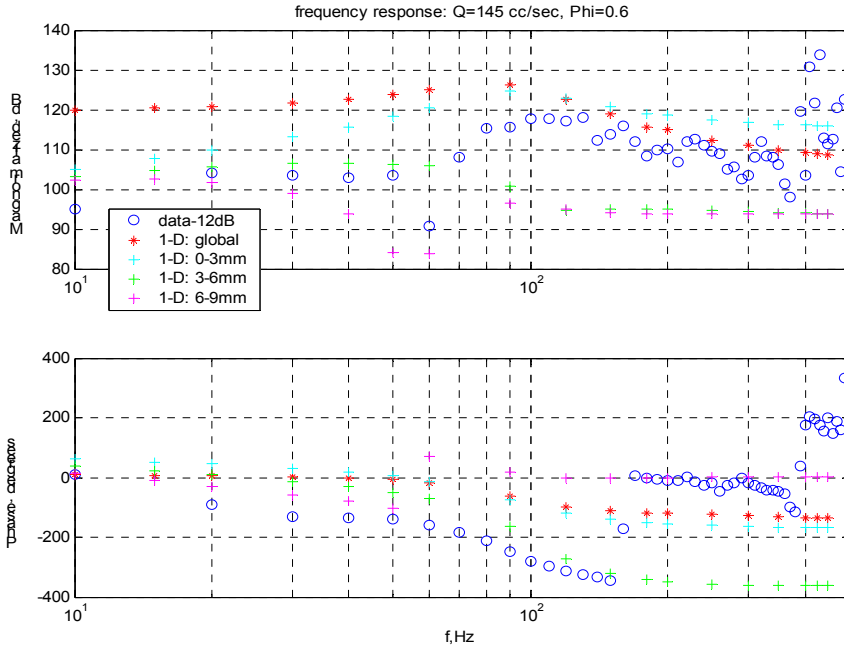


(e) Q=200 cc/sec, $\Phi=0.75$

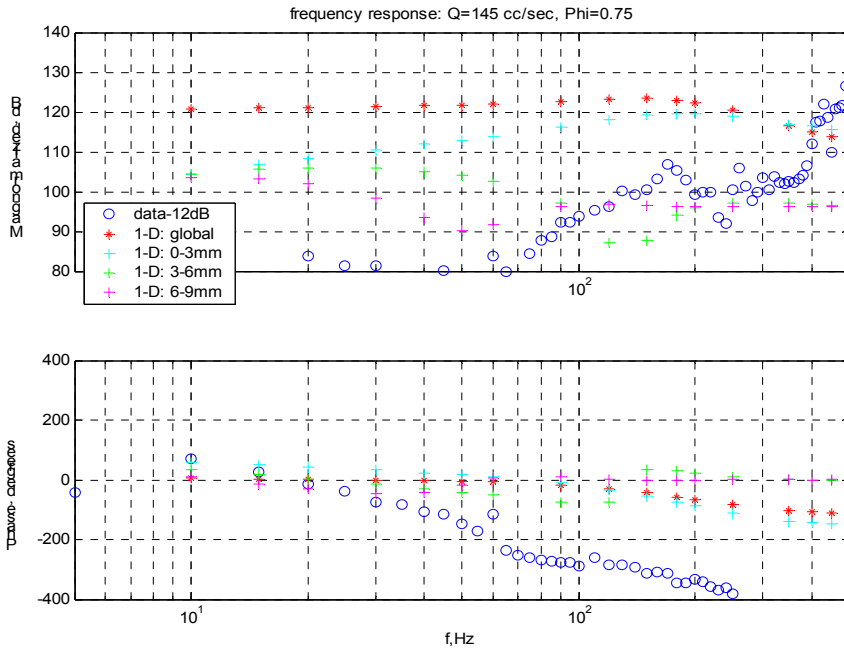
Figure 4.16. Numerical Flame Model. The numerical model predicts the frequency responses well for most cases.



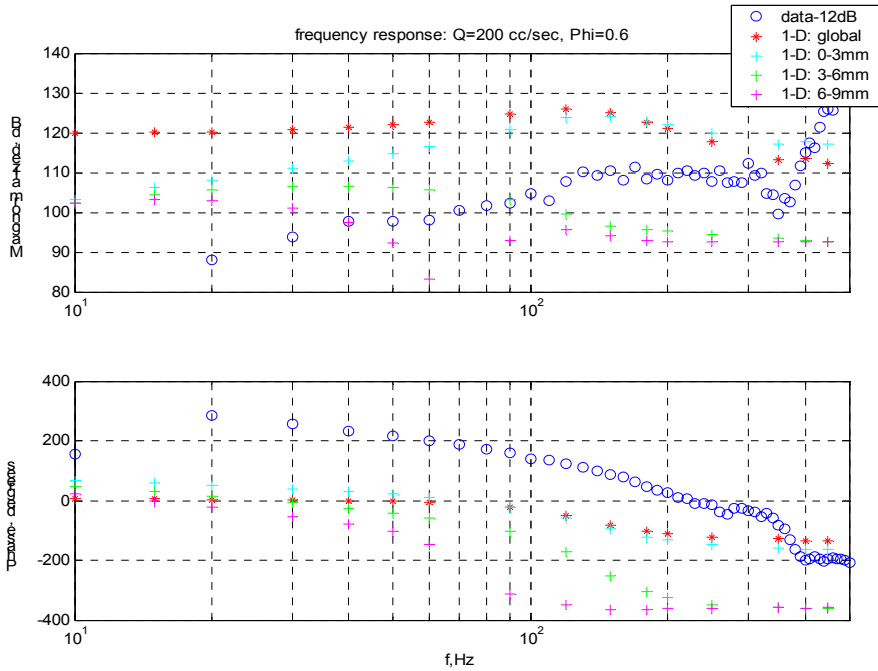
(a) Q=145 cc/sec, $\Phi=0.55$



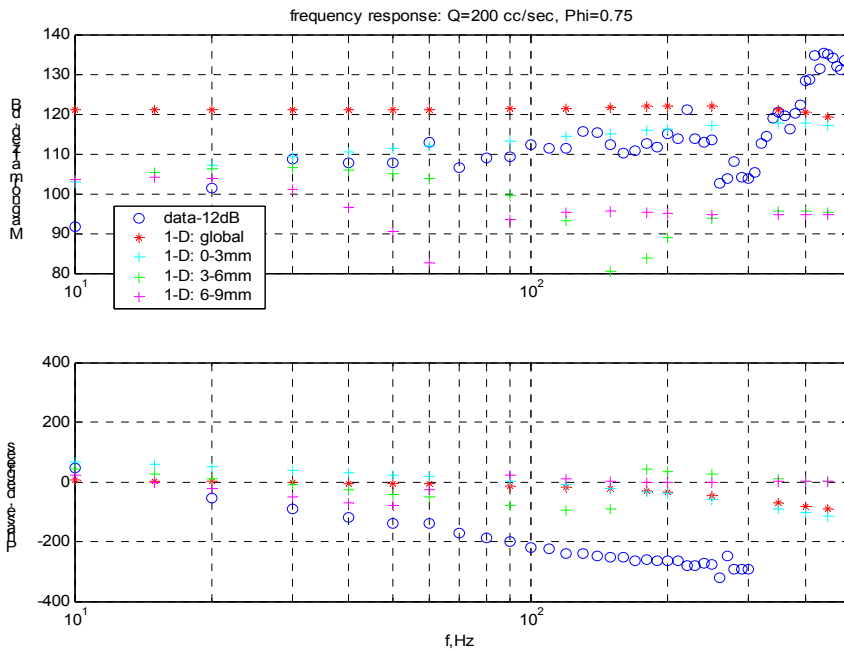
(b) Q=145 cc/sec, $\Phi=0.60$



(c) Q=145 cc/sec, $\Phi=0.75$



(d) Q=200 cc/sec, $\Phi=0.60$



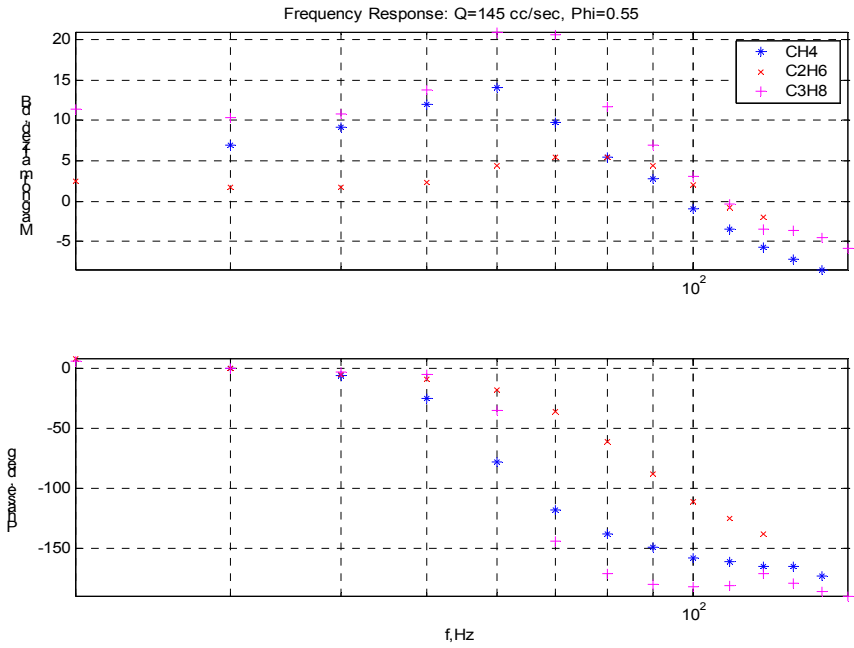
(e) Q=200 cc/sec, $\Phi=0.75$

Figure 4.17. Local v. Global Frequency Response Function. The frequency response is dependent on measurement location.

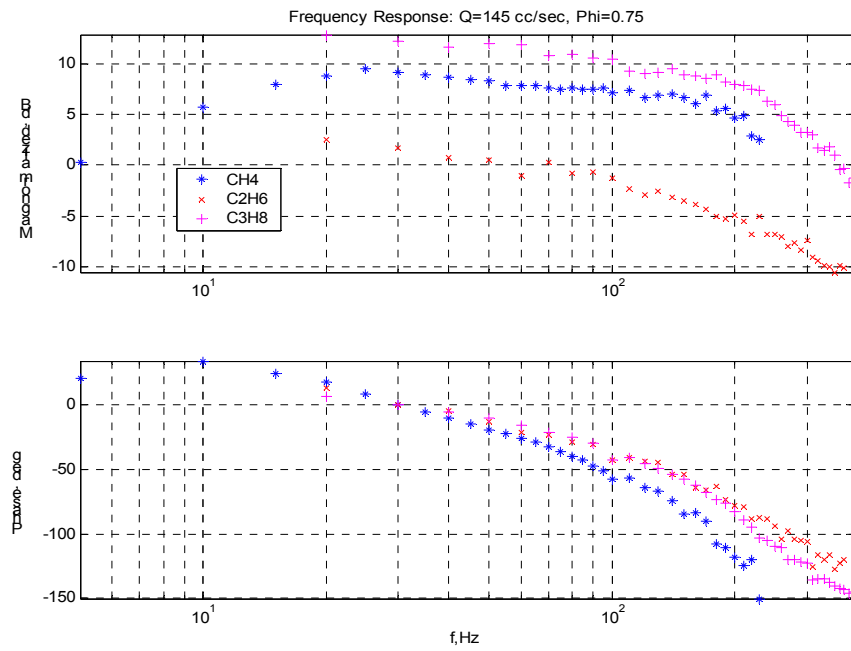
4.3.7 Fuel variability. The properties of the fuel have a significant effect on the flame dynamics. Differing flame speeds affect the bandwidth of chemical kinetics. Heating values, indicative of the chemical energy contained in the model, affect the dynamic gain. The molecular weight, heat of formation, adiabatic flame temperature, and adiabatic flame speed of the fuels studied are summarized in Table 4.18. From the OH* chemiluminescence frequency response data, shown in Figure 4.19, it is evident that at low equivalence ratios, the bandwidth of reaction rate scales roughly with adiabatic flame speed. Damping also roughly scales inversely with flame speed. At high equivalence ratios, the difference is primarily a gain term, with propane showing the highest gain and ethane the lowest. These trends are carried to the temperature frequency responses, shown in Figure 4.20. Here, though, gain is most likely affected by the relative location of the flame and measurement volume. Since methane has the lowest flame speed, the flame would be located farthest away from the honeycomb (closest to the measurement volume), so the gain is highest in this case.

Table 4.18. Fuel Properties. Methane, ethane, and propane were studied [10].

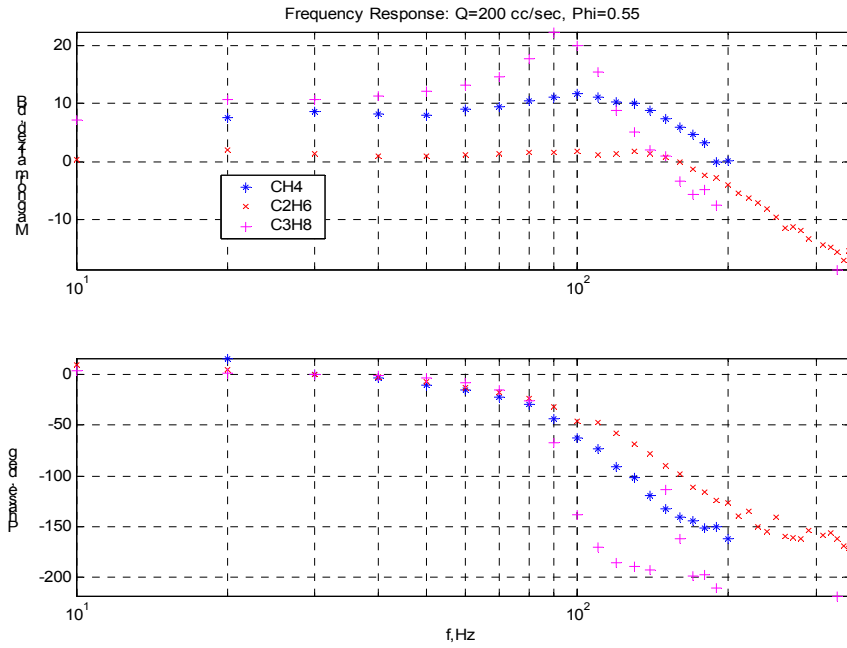
Formula	Fuel	MW [kg/kmol]	h_f^0 [kJ/kmol]	T_{ad} [K]	$S_{L,ad}$ [cm/s]
CH ₄	Methane	16.043	-74831	2226	40
C ₂ H ₆	Ethane	30.069	-84667	2259	43
C ₃ H ₈	Propane	44.096	-103847	2267	44



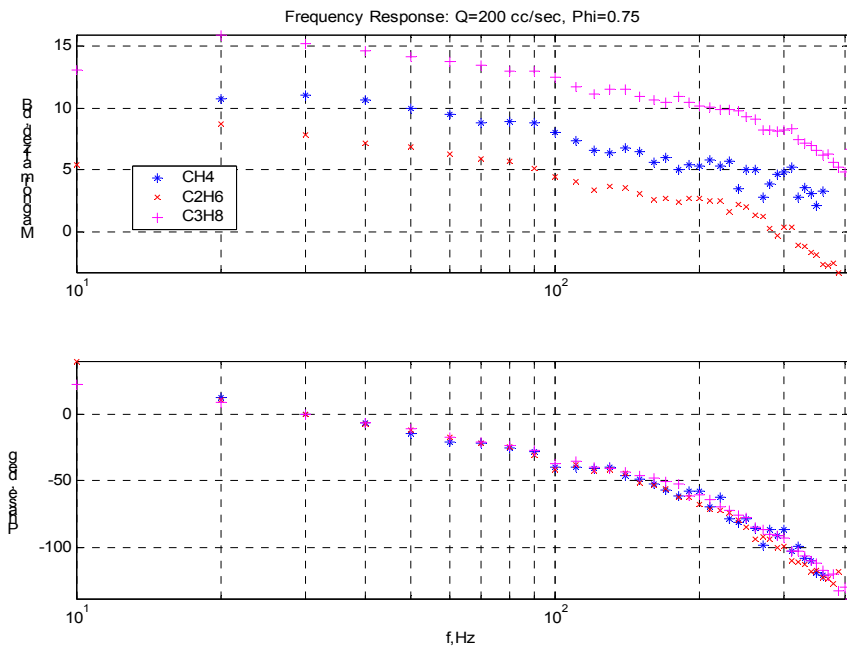
(a) Q=145 cc/sec, $\Phi = 0.55$



(b) Q=145 cc/sec, $\Phi = 0.75$

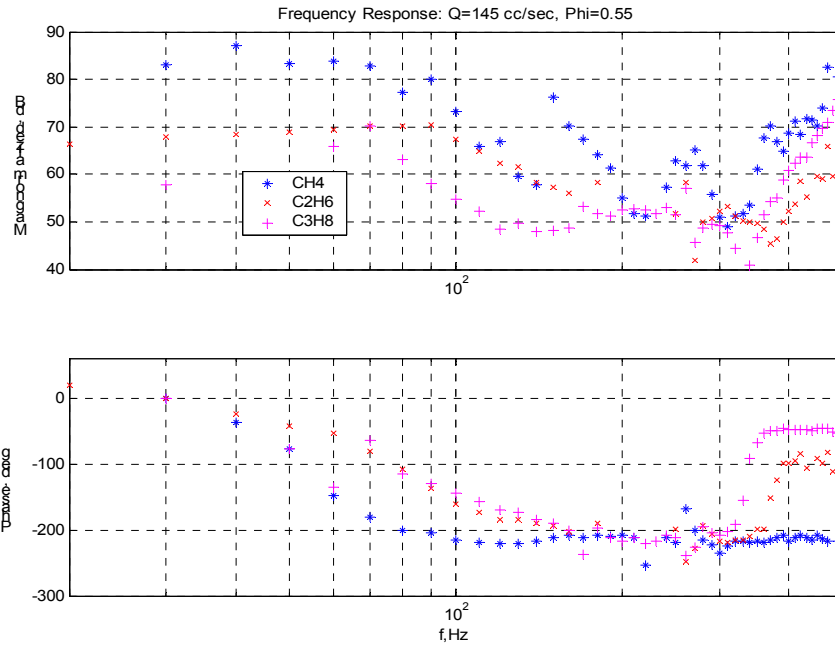


(c) $Q=200$ cc/sec, $\Phi = 0.55$

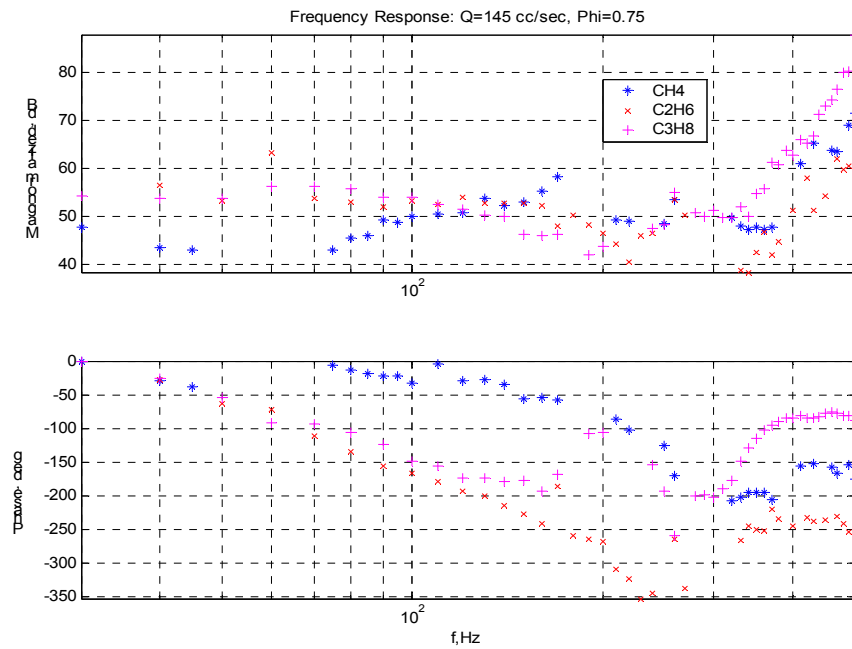


(d) $Q=200$ cc/sec, $\Phi = 0.75$

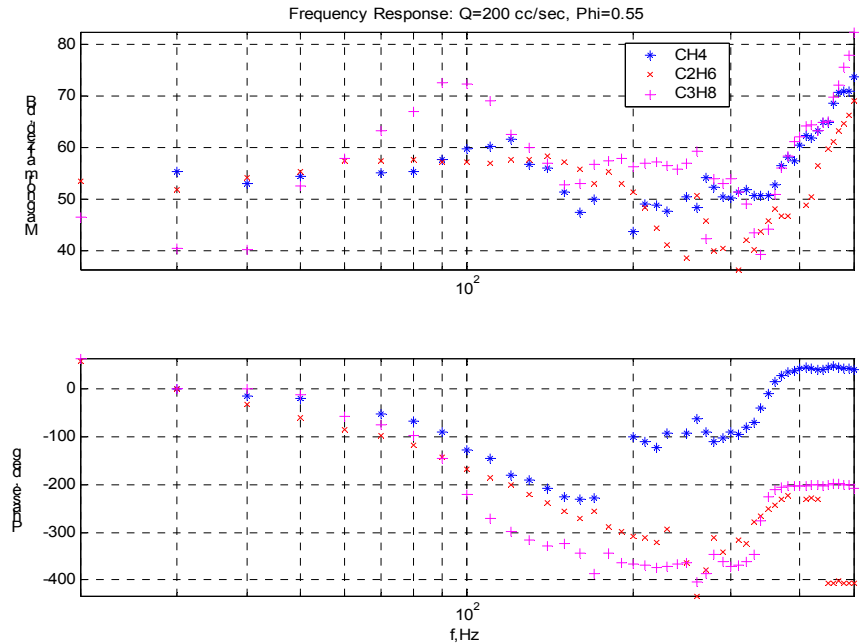
Figure 4.19. Fuel Variability – OH* FRF. Fuel properties affect the flame dynamics.



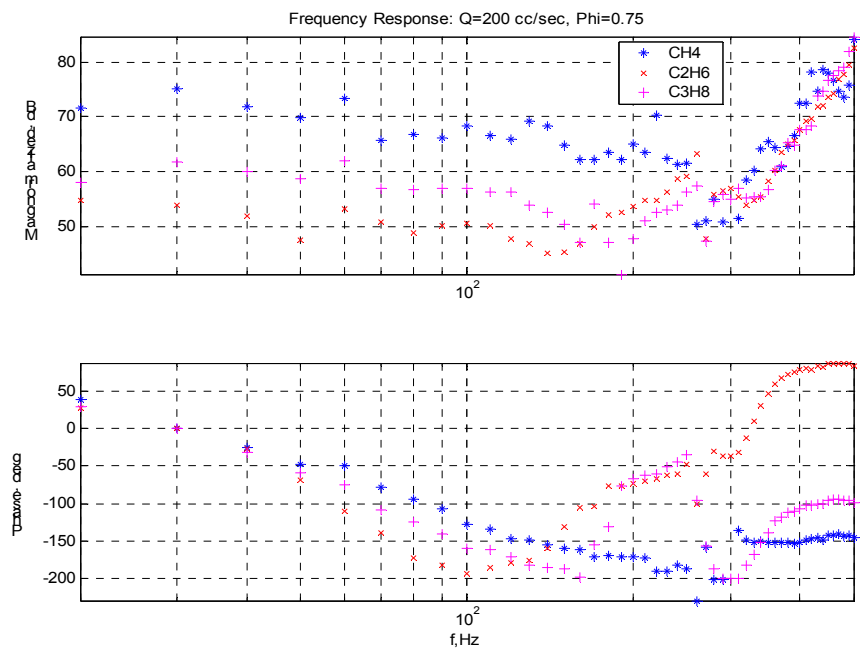
(a) Q=145 cc/sec, $\Phi = 0.55$



(b) Q=145 cc/sec, $\Phi = 0.75$



(c) Q=200 cc/sec, $\Phi = 0.55$



(d) Q=200 cc/sec, $\Phi = 0.75$

Figure 4.20. Fuel Variability – Temperature FRF. Properties of the fuel affect the transient response.

4.4 Models of Laminar Flame Dynamics

4.4.1. Approach. This aspect of the study focuses on an empirical approach to developing low-order models of flame dynamics. First, an analytical and numerical analysis yields the physical processes that must be measured to capture the acoustic forcing function. Next, measurement techniques are devised to measure the dominant processes, in this case OH* chemiluminescence, product gas temperature, velocity fluctuations, and equivalence ratio fluctuations. Frequency response functions are then measured of the OH* chemiluminescence and product gas temperature with respect to velocity fluctuations. A subsequent study will measure the frequency response functions with respect to equivalence ratio. Through performing a dimensional analysis of the conservation equations, groupings of the dominant parameters are found. The data is plotted non-dimensionally using these parameters. Finally, low-order dynamic models are fit to the scaled frequency response data.

4.4.2 Dimensional Analysis. A dimensional analysis was performed on the conservation equations to find dimensionless groups of parameters by which the data can be scaled. The resulting dimensionless groups can be used as variables in the low-order models.

From Kuo [11], the 1-D continuity, momentum, and energy equations are:

$$\frac{\partial p}{\partial t} + \frac{\partial(\rho u)}{\partial x} = 0 \quad (4.1)$$

$$\rho \frac{\partial u}{\partial t} + \rho u \frac{\partial u}{\partial x} = -\frac{\partial p}{\partial x} + \frac{\partial \tau_{xx}}{\partial x} + B_x \quad (4.2)$$

$$\begin{aligned} \rho C_p \left(\frac{\partial T}{\partial t} + u \frac{\partial T}{\partial x} \right) - \left(\frac{\partial p}{\partial t} + u \frac{\partial p}{\partial x} \right) = \\ \lambda \frac{\partial^2 T}{\partial x^2} - \sum_{i=1}^N \omega_i h_i^0 - \frac{\partial}{\partial x} \left(\rho T \sum C_{p,i} Y_i v_i \right) + \mu \left[2 \left(\frac{\partial u}{\partial x} \right)^2 - \frac{2}{3} \left(\frac{\partial u}{\partial x} \right)^2 \right] + \rho \sum_{i=1}^N Y_i f_{x,i} v_i \end{aligned} \quad (4.3)$$

If kinetic energy, viscous forces, and body forces (other than the buoyancy force) are neglected, the momentum and energy equations simplify to:

$$\rho \frac{\partial u}{\partial t} + \rho u \frac{\partial u}{\partial x} + \frac{\partial p}{\partial x} = \rho g \quad (4.4)$$

$$\rho C_p \left(\frac{\partial T}{\partial t} + u \frac{\partial T}{\partial x} \right) = \lambda \frac{\partial^2 T}{\partial x^2} - \sum_{i=1}^N \omega_i h_i^0 - h \frac{\partial T}{\partial x} - \epsilon \sigma \frac{\partial (T^4)}{\partial x} \quad (4.5)$$

The reference quantities are then chosen as:

$$u_0 = \text{flame speed} \left[\frac{m}{s} \right]$$

$$t_0 = \text{period of oscillation} [s]$$

$$T_0 = \text{ambient temperature} [K]$$

$$P_0 = \text{atmospheric pressure} [Pa]$$

$$l_0 = \text{burner radius} [m]$$

$$\rho_0 = \frac{P_0}{RT_0} \left[\frac{kg}{m^3} \right]$$

$$h_o = C_p T_0 \left[\frac{J}{kg} \right]$$

$$\dot{\omega}_0 = \text{reaction rate at steady-state} \left[\frac{kg}{s \cdot m^3} \right]$$

$$h_{conv,0} = \text{heat transfer coefficient (convective)} \left[\frac{W}{m^2 \cdot K} \right]$$

$$\sigma_0 = \text{Stefan-Boltzman coefficient (radiative)} \left[\frac{W}{m^2 \cdot K^4} \right]$$

$$\lambda_0 = \text{thermal conductivity} \left[\frac{W}{m \cdot K} \right]$$

The non-dimensional quantities are then given as:

$$u^* = \frac{u}{u_0}, A^* = \frac{A}{\pi l_0^2}, C_p^* = \frac{C_p}{h_0/T_0}, \dot{m}^* = \frac{\dot{m}}{\rho_0 \pi l_0^2 u_0}, h_i^* = \frac{h_i}{C_p T_0}, \dots$$

Substituting these quantities into the conservation equations, the result is:

$$\frac{\partial \rho^*}{\partial t^*} + \frac{t_0 u_0}{l_0} \frac{\partial (\rho^* u^*)}{\partial x^*} = 0 \quad (4.6)$$

$$\frac{l_0}{u_0 t_0} \rho^* \frac{\partial u^*}{\partial t^*} + \rho^* u^* \frac{\partial u^*}{\partial x^*} + \frac{p_0}{\rho_0 u_0^2} \frac{\partial p^*}{\partial x^*} = \frac{g l_0}{u_0^2} \quad (4.7)$$

$$\begin{aligned} & \rho^* C_p^* \left(\frac{\partial T^*}{\partial t^*} + \frac{t_0 u_0}{l_0} u^* \frac{\partial T^*}{\partial x^*} \right) = \\ & \frac{\lambda_0 t_0}{\rho_0 C_{p,0} l_0^2} \lambda^* \frac{\partial^2 T^*}{\partial x^{*2}} - \sum_{i=1}^N \frac{\dot{\omega}_{i,0} t_0}{\rho_0} \omega_i^* h_i^* - \frac{h_{conv,0} t_0}{l_0 \rho_0 C_{p,0}} h^* \frac{\partial T^*}{\partial x^*} - \frac{\sigma_0 T_0^3 t_0}{l_0 \rho_0 C_{p,0}} \epsilon \sigma^* \frac{\partial (T^{*4})}{\partial x^*} \end{aligned} \quad (4.8)$$

The non-dimensional form of the equation yields non-dimensional parameters as coefficients. Further groupings can be derived through ratios of the coefficients.

$$\text{Strouhal} = \frac{l_0}{u_0 t_0}$$

$$\text{Euler} = \frac{p_0}{\rho_0 u_0^2}$$

$$\text{Nusselt} = \frac{h_{conv,0} l_0}{\lambda_0} = \frac{\text{convective}}{\text{diffusive}}$$

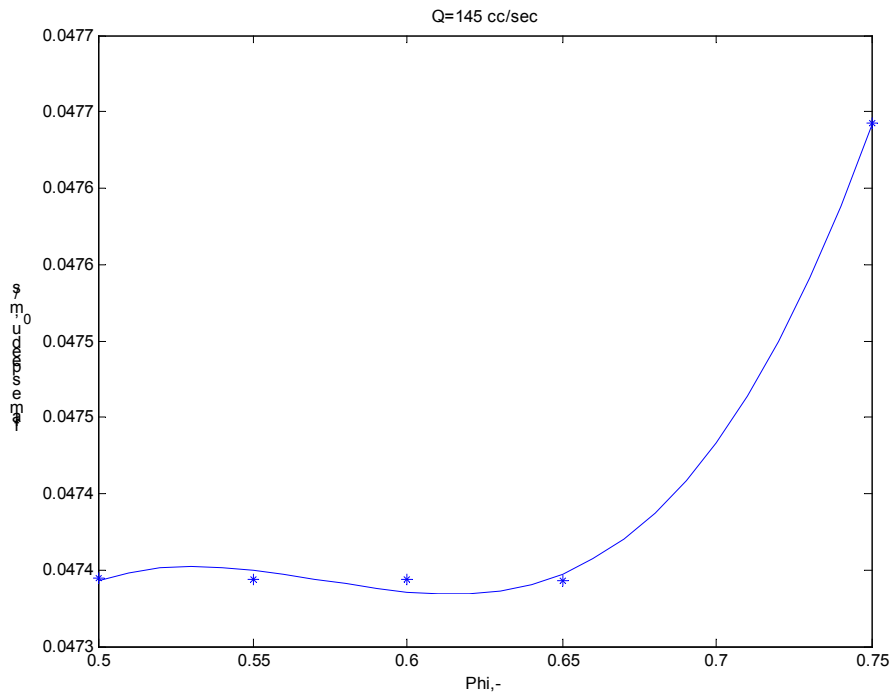
$$\text{Froude} = \frac{u_0}{\sqrt{g l_0}}$$

$$\text{Damkohler} = \frac{h_0}{\dot{\omega}_0 l_0 C_{p,0}} = \frac{\text{convective}}{\text{chemical}}$$

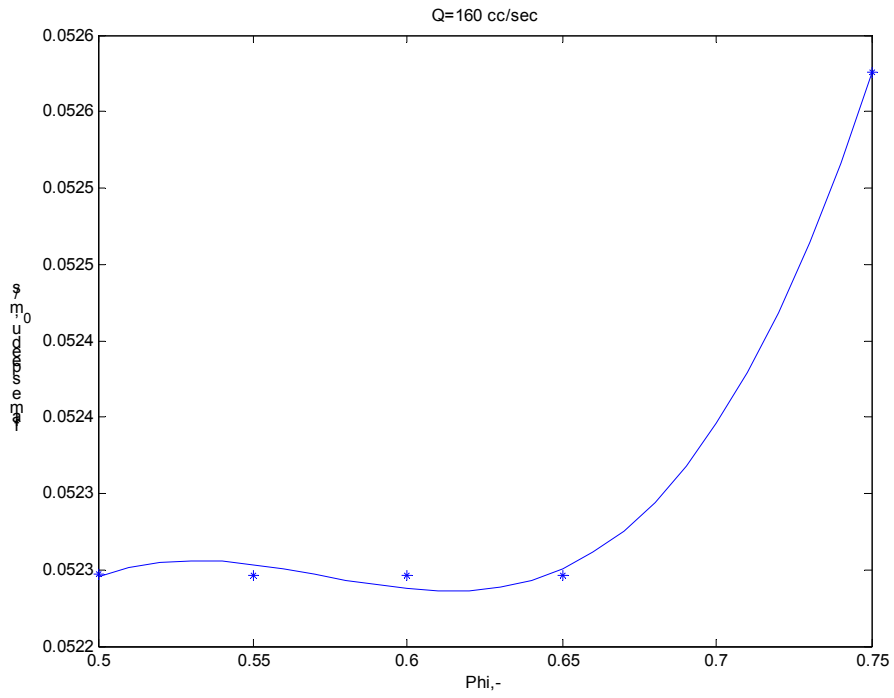
$$\frac{\sigma_0 T_0^3 l_0}{\lambda_0} = \frac{\text{radiative}}{\text{diffusive}}$$

The above groupings agree with those found in the literature [12, 13]. For instance, if the reference length is chosen as the flame length, L_f , instead of the burner radius, the flame Strouhal number $St_{flame} = fL_f / \bar{u}$ used by Lieuwen is found [7]. Candel bases flame dynamics models on a form of the Strouhal number above $\omega^* = \omega R / (S_L \cos \alpha)$, where α is the half angle of the flame and R is the radius of the burner [14]. If the forms of the conservation equations used include all of the relevant processes, these parameters represent the dominant variables for flame dynamics.

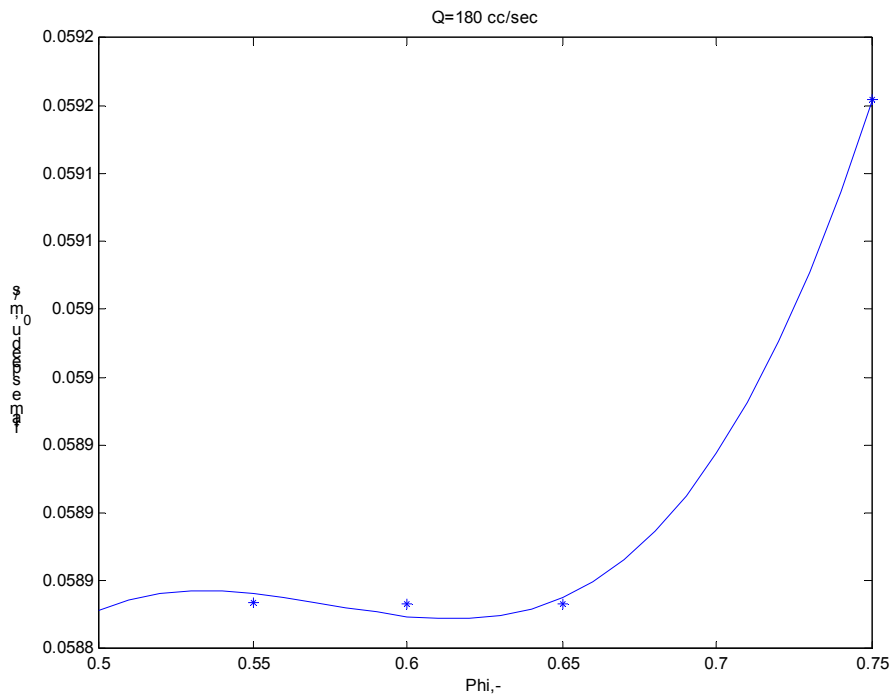
The laminar flame speed was needed to calculate dimensionless parameters. For methane, the flame speed, u_0 , was calculated using the laminar flame code (see section 4.3.6). Correlations were then fit to the code data as shown in Figure 4.21. For ethane and propane, the flame speed calculated from the code, for methane, was scaled using the ratio of adiabatic laminar flame speeds.



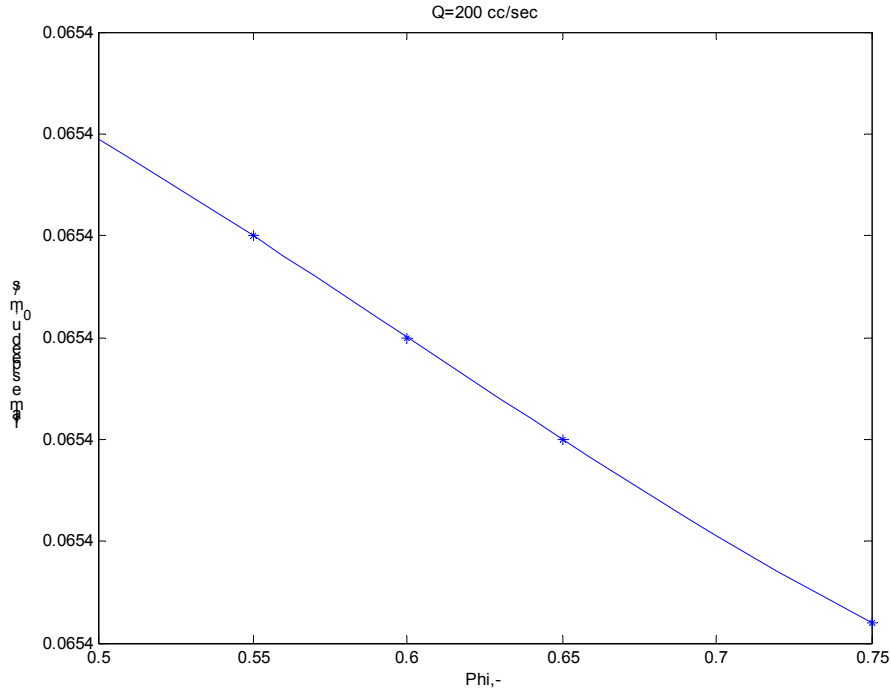
(a) Q=145 cc/sec



(b) Q=160 cc/sec



(c) Q=180 cc/sec



(d) Q=200 cc/sec

Figure 4.21. Laminar Flame Speed for Methane. The flame speed varies with equivalence ratio.

4.4.3 Case Models. Using the parameters from the dimensional analysis, the frequency response functions were plotted in non-dimensional form. The OH* chemiluminescence frequency response functions were normalized using

$$M^* = \frac{OH^* / OH_{ss}^*}{u / u_0}$$

where the steady-state OH* chemiluminescence values are shown in Table 4.22. The temperature frequency responses were normalized using

$$M^* = \frac{T / T_{ss}}{u / u_0}$$

The temperature is scaled by the steady state temperature, T_{ss} , or the mean of the temperature measured at the beginning and end of each test. The steady-state

temperatures are shown in Table 4.28. The abscissa was normalized using the Strouhal number,

$$St = \frac{l_0}{u_0 t_0} = \frac{\omega R}{u_0}.$$

When plotted in dimensionless terms, the data becomes much more compact. From the approximately 180 degrees of phase drop, it is evident the frequency responses best fit a second-order system. A Matlab ® code, tranfit.m, was written that allows the user to input a transfer function, in terms of time delay, real and complex zeros, and real and complex poles. The user can then iterate on the initial guess. Once the user is satisfied with the initial guess, the program optimizes the parameters of the transfer function to fit the data. Using this technique, transfer functions were fit to the data in the form

$$H_f(j\omega^*) = H_f(s^*) = \frac{Ke^{-s^*\tau}}{s^{*2} + 2\zeta\omega_n^* s^* + \omega_n^{*2}} \quad (4.9)$$

where $\omega^* = St$, K is the gain, τ is the time delay, ζ is the damping ratio, and ω_n^* is the dimensionless resonant frequency.

The model parameters for reaction rate dynamics are shown in Table 4.23 and plotted in Figure 4.24. As observed in the raw data, natural frequency and damping ratio increase with equivalence ratio and flow rate. The models are plotted against the data in Figures 4.25, 4.26, and 4.27 for methane, ethane, and propane. Note that peaks in magnitude attributed to 2-D effects (see section 4.3.4) were not fitted. Also, these are relatively simple models. Therefore, all of the relevant physics are not captured. However, the dominant dynamics are well described by these low-order, compact models.

Table 4.22. Steady-state OH* levels [V].

(a) Methane

Phi, -	Q=145 cc/sec	Q=160 cc/sec	Q=180 cc/sec	Q=200 cc/sec
0.50	0.01303	0.03465	0.01714	0.01697
0.55	0.01233	0.02156	0.00676	0.01047
0.60	0.03283	0.03018	0.02583	0.00765
0.65	0.01862	0.02463	0.02094	0.02058
0.75	0.02374	0.03088	0.01932	0.03774

(b) Ethane

Phi, -	Q=145 cc/sec	Q=200 cc/sec
0.55	0.0110	0.0144
0.75	0.0568	0.0333

(c) Propane

Phi, -	Q=145 cc/sec	Q=200 cc/sec
0.55	0.0176	0.0218
0.75	0.0299	0.0289

Table 4.23. Dynamic Models of Chemical Heat Release Rate.

(a) Methane

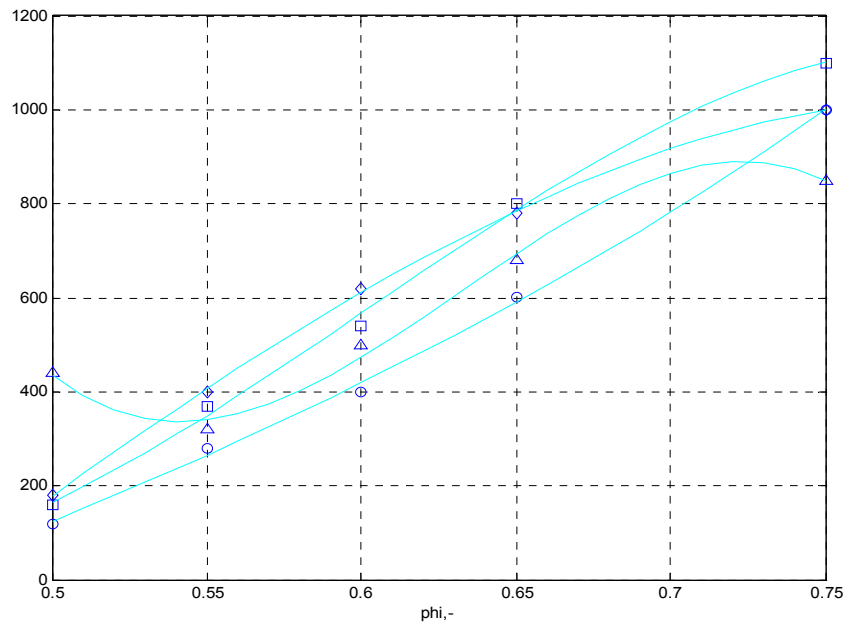
Q, cc/sec	Phi, -	K	Tau	wn*	Z
145	0.50	8.0E+05	3.0E-04	120	0.28
	0.55	4.0E+06	3.0E-04	280	0.20
	0.60	3.0E+06	3.0E-04	400	0.20
	0.65	1.0E+07	3.0E-04	600	0.35
	0.75	2.2E+07	6.0E-04	1000	0.45
160	0.50	4.5E+06	4.0E-04	440	0.35
	0.55	4.0E+06	4.0E-04	320	0.23
	0.60	5.0E+06	4.0E-04	500	0.28
	0.65	1.1E+07	2.0E-04	680	0.38
	0.75	1.8E+07	3.0E-04	850	0.55
180	0.50	1.5E+06	4.0E-04	160	0.17
	0.55	1.5E+07	3.0E-04	370	0.25
	0.60	1.0E+07	3.0E-04	540	0.40
	0.65	2.0E+07	3.0E-04	800	0.50
	0.75	3.7E+07	3.0E-04	1100	0.50
200	0.50	2.5E+06	3.0E-04	180	0.15
	0.55	1.5E+07	2.0E-04	400	0.30
	0.60	3.5E+07	2.0E-04	620	0.40
	0.65	2.0E+07	2.0E-04	780	0.45
	0.75	2.0E+07	2.0E-04	1000	0.45

(b) Ethane

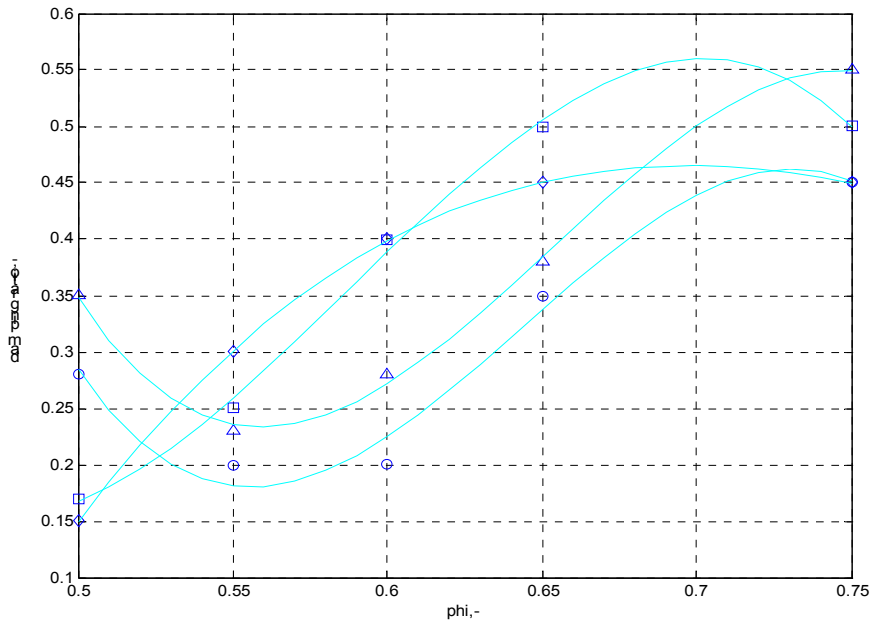
Q, cc/sec	Phi, -	K	Tau	wn*	Z
145	0.55	4.0E+06	2.0E-04	380	0.23
	0.75	4.0E+06	0.0E+00	800	0.80
200	0.55	6.0E+06	0.0E+00	450	0.35
	0.75	1.4E+07	0.0E+00	800	0.70

(c) Propane

Q, cc/sec	Phi, -	K	Tau	wn*	Z
145	0.55	4.00E+06	0.00E+00	260	0.06
	0.75	2.40E+07	0.00E+00	900	0.5
200	0.55	4.00E+06	2.00E-04	275	0.06
	0.75	4.20E+07	0.00E+00	800	0.7



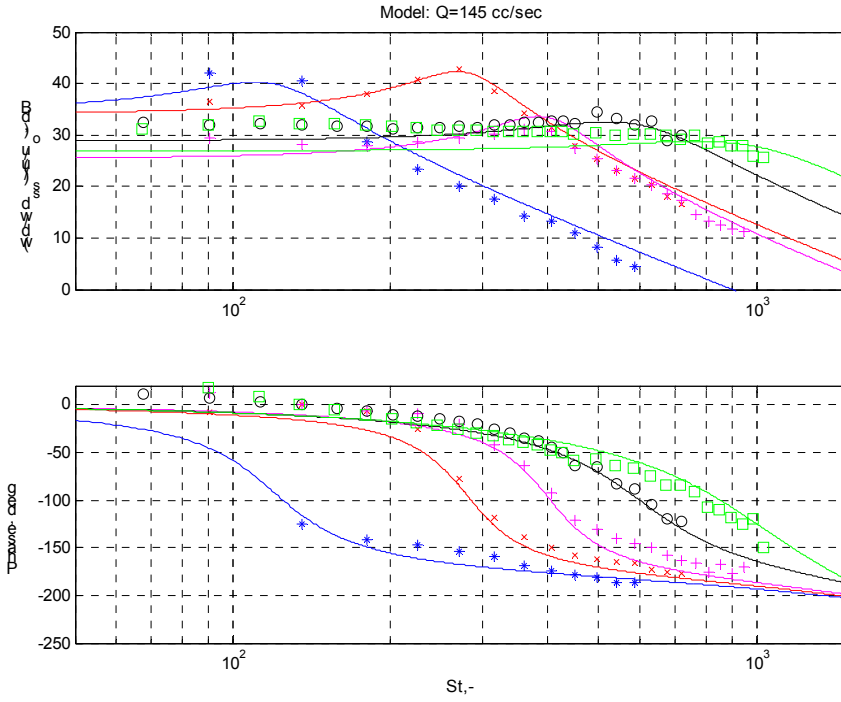
(a) natural frequency



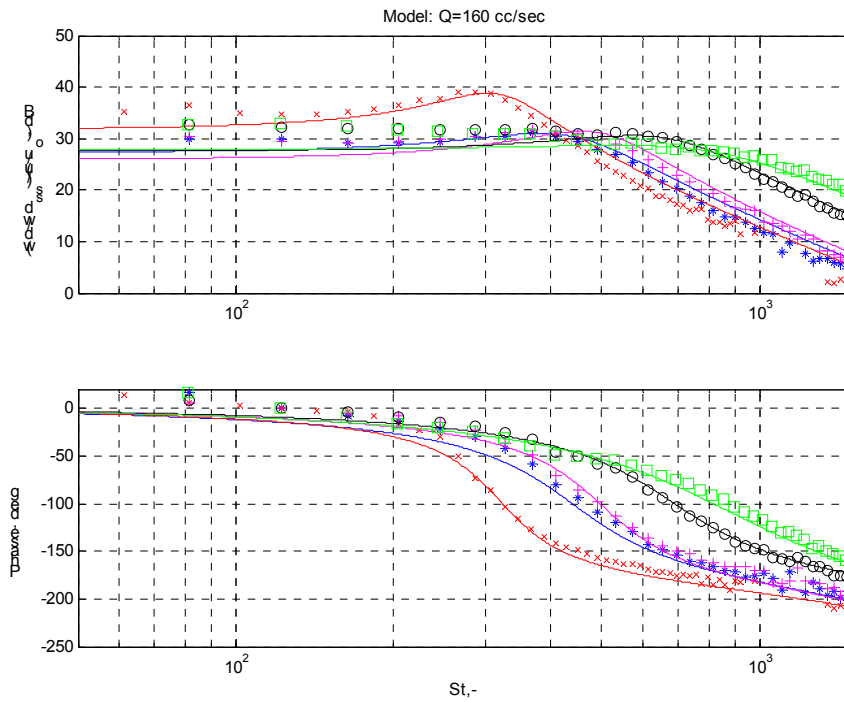
(b) damping ratio

Figure 4.24. Parameters of the Dynamic Models of Chemical Heat Release Rate.

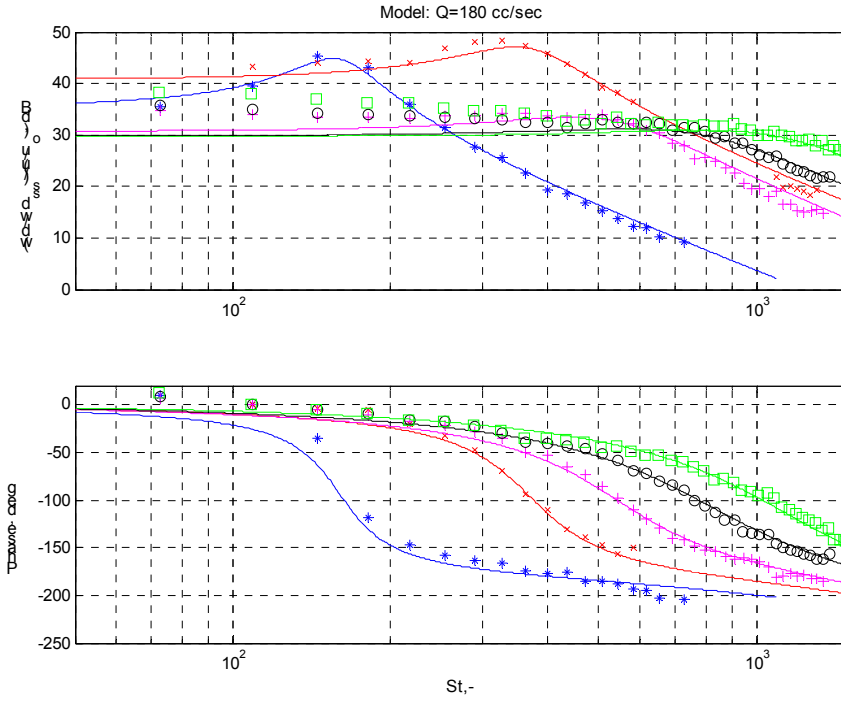
Flow rates [cc/sec]: ○ 145, △ 160, □ 180, ◇ 200.



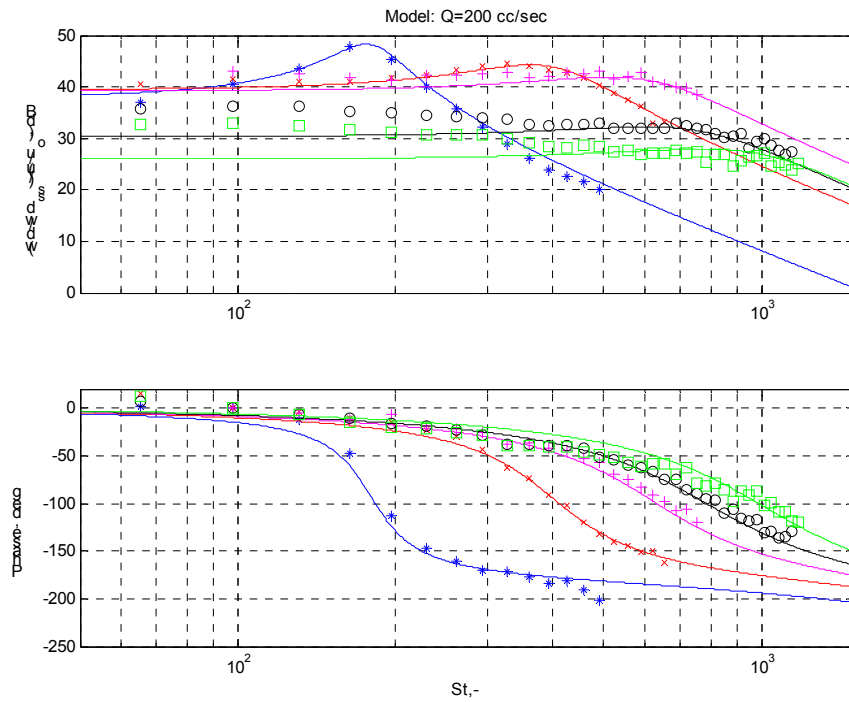
(a) Q=145 cc/sec



(b) Q=160 cc/sec

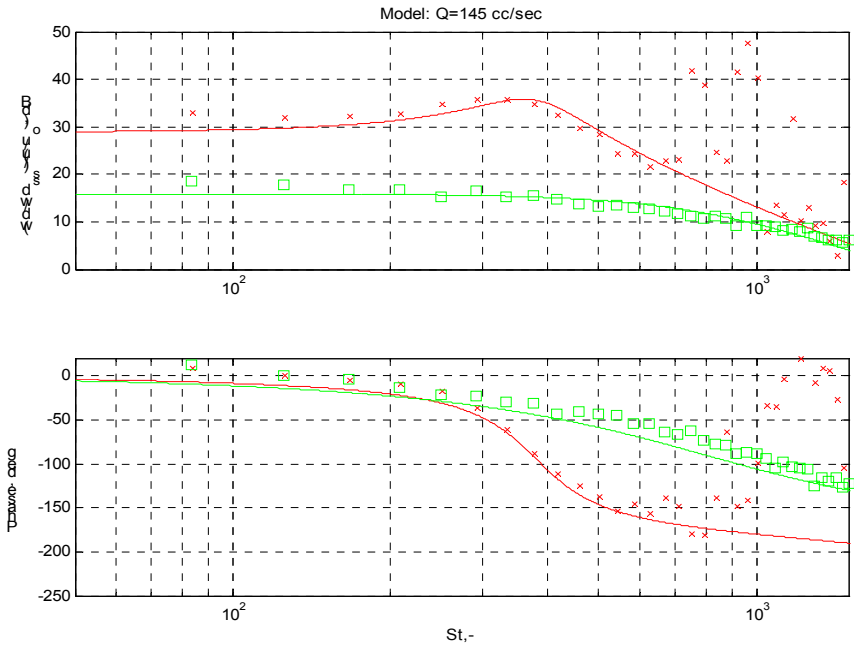


(c) Q=180 cc/sec

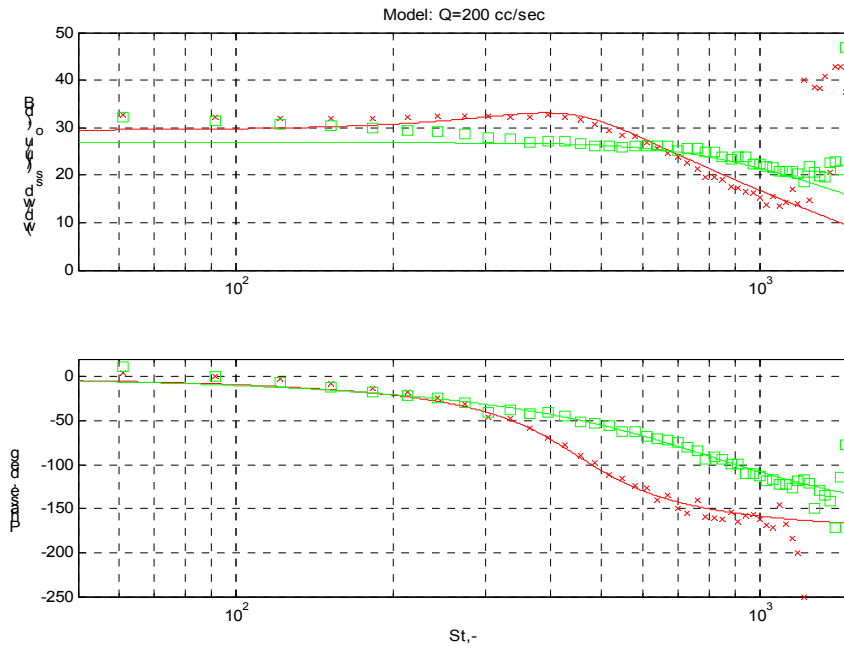


(d) Q=200 cc/sec

Figure 4.25. Dynamic Models of Chemical Heat Release Rate for Methane.

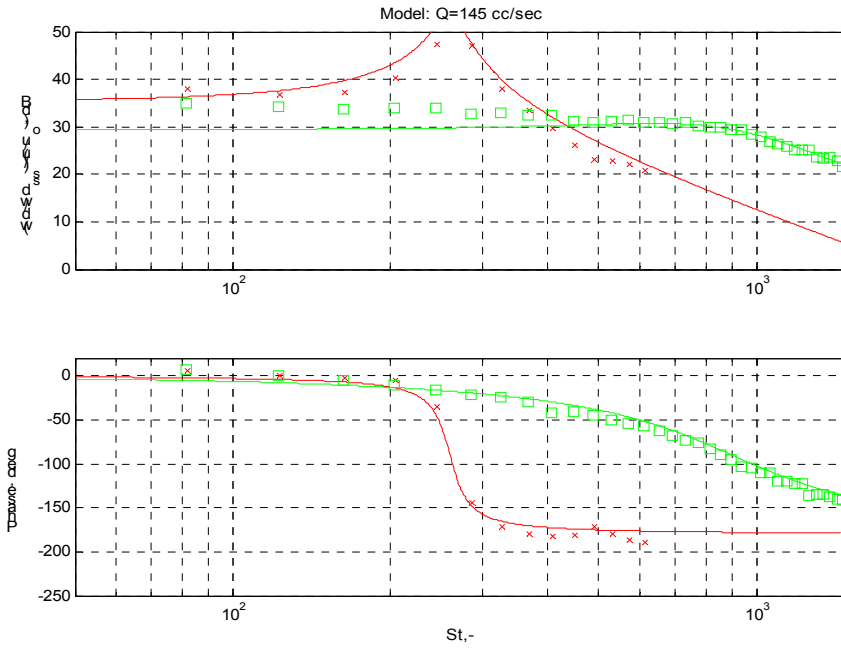


(a) Q=145 cc/sec

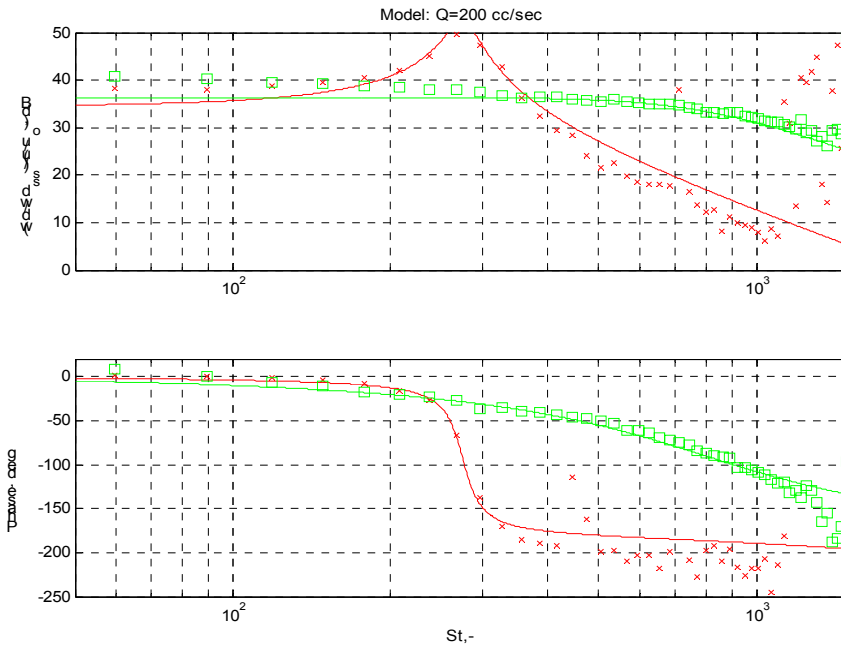


(b) Q=200 cc/sec

Figure 4.26. Dynamic Models of Chemical Heat Release Rate for Ethane.



(a) Q=145 cc/sec



(b) Q=200 cc/sec

Figure 4.27. Dynamic Models of Chemical Heat Release Rate for Propane.

Models of acoustic forcing function dynamics were constructed in a similar manner using the dynamic temperature frequency responses. The steady-state temperatures are shown in Table 4.28. The model parameters for acoustic forcing function dynamics are shown in Table 4.29 and plotted in Figure 4.30. As in the models of reaction rate, natural frequency and damping ratio increase with equivalence ratio and flow rate. The acoustic forcing function data collapses better than the reaction rate data. The models are plotted against the data in Figures 4.31, 4.32, and 4.33 for methane, ethane, and propane.

Table 4.28. Steady-State Temperature. The steady-state temperature was measured at the beginning and end of each test.

(a) Methane

Phi, -	Q=145 cc/sec	Q=160 cc/sec	Q=180 cc/sec	Q=200 cc/sec
0.50	1311.59	1677.51	1588.53	1669.78
	1311.59	1642.20	1600.12	1457.53
0.55	1616.22	2407.33	2339.79	1533.08
	1616.22	2407.33	2520.38	1585.30
0.60	1808.47	1993.54	1547.03	1590.00
	1837.71	1993.54	1479.84	1579.31
0.65	1749.19	2244.23	2120.70	1570.64
	1683.15	2244.23	2120.70	1592.51
0.75	1703.76	1607.97	2160.73	1588.81
	1679.69	1635.25	2138.97	1651.12

(b) Ethane

Phi, -	Q=145 cc/sec	Q=200 cc/sec
0.55	1834.04	1819.94
	1884.73	1882.85
0.75	1823.40	1774.96
	1920.73	1843.35

(c) Propane

Phi, -	Q=145 cc/sec	Q=200 cc/sec
0.55	1603.73	1680.92
	1650.23	1921.86
0.75	1669.07	1852.40
	1669.07	1734.83

Table 4.29. Parameters of the Dynamic Models of Acoustic Forcing Function.
Second-order models with time delay approximate the data.

(a) Methane

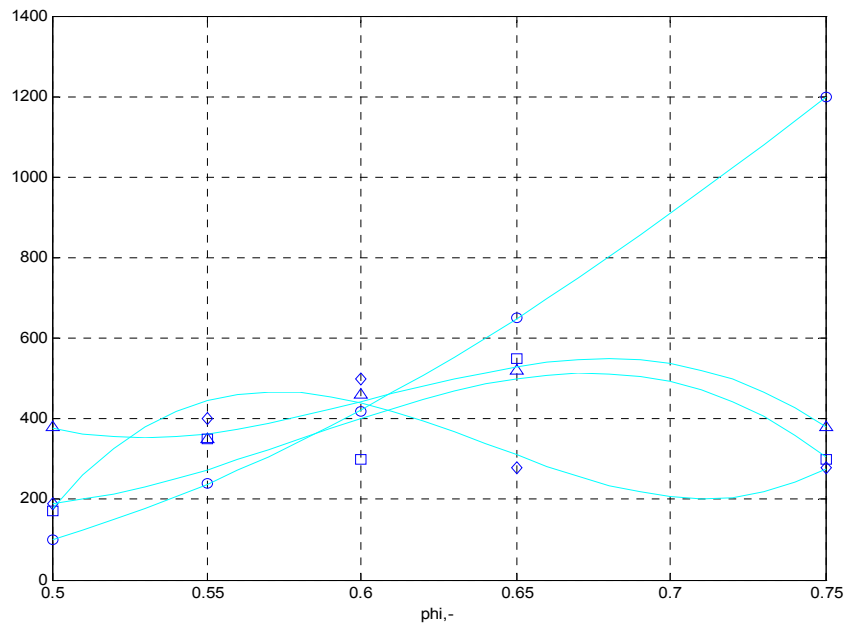
Q, cc/sec	Phi, -	K	Tau	wn*	Z
145	0.50	3.0E+04	1.0E-04	100	0.30
	0.55	1.0E+05	1.0E-03	240	0.12
	0.60	8.0E+04	1.5E-03	420	0.18
	0.65	4.0E+04	5.0E-04	650	0.30
	0.75	5.0E+04	0.0E+00	1200	0.50
	0.50	5.0E+04	5.0E-04	380	0.30
160	0.55	1.5E+05	1.0E-03	350	0.25
	0.60	7.0E+04	2.3E-03	460	0.20
	0.65	4.0E+05	2.3E-03	520	0.43
	0.75	3.0E+05	1.5E-03	380	0.60
180	0.50	7.0E+04	1.0E-04	170	0.30
	0.55	4.0E+04	2.5E-03	350	0.10
	0.60	3.5E+04	1.0E-03	300	0.35
	0.65	3.0E+05	2.3E-03	550	0.45
	0.75	7.0E+04	8.0E-04	300	0.60
	0.50	3.0E+04	6.0E-04	190	0.15
200	0.55	2.0E+04	3.0E-03	400	0.20
	0.60	7.0E+04	2.5E-03	500	0.30
	0.65	7.0E+04	1.5E-03	280	0.50
	0.75	7.0E+04	5.0E-04	280	0.40

(b) Ethane

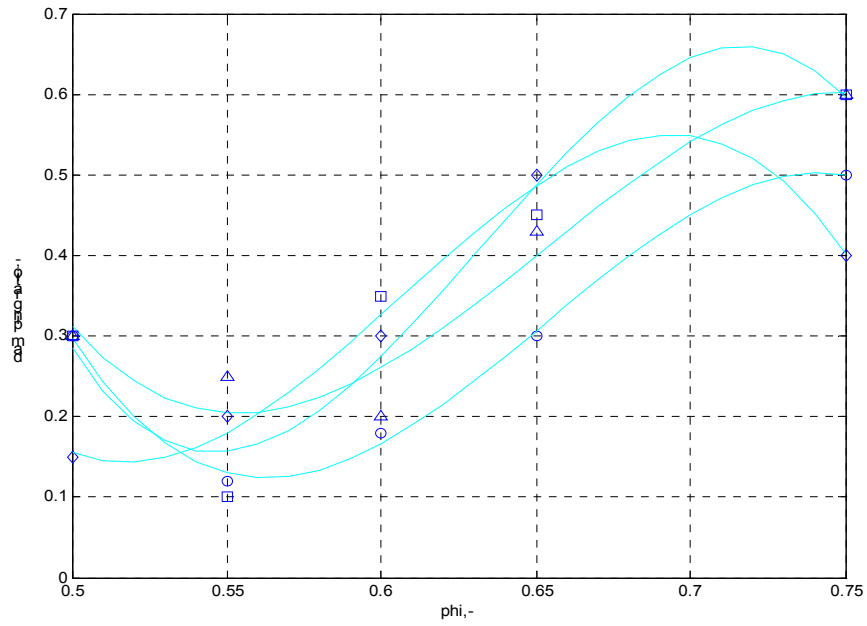
Q, cc/sec	Phi, -	K	Tau	wn*	Z
145	0.55	5.0E+04	1.2E-03	350	0.30
	0.75	4.0E+04	3.5E-03	650	0.60
200	0.55	2.0E+04	4.5E-03	350	0.40
	0.75	1.0E+04	3.5E-03	350	0.60

(c) Propane

Q, cc/sec	Phi, -	K	Tau	wn*	Z
145	0.55	4.00E+04	1.50E-03	350	0.6
	0.75	1.50E+04	1.50E-03	350	0.5
200	0.55	1.00E+09	5.00E-04	290 (2)	0.2
	0.75	2.00E+04	2.50E-03	250	0.5

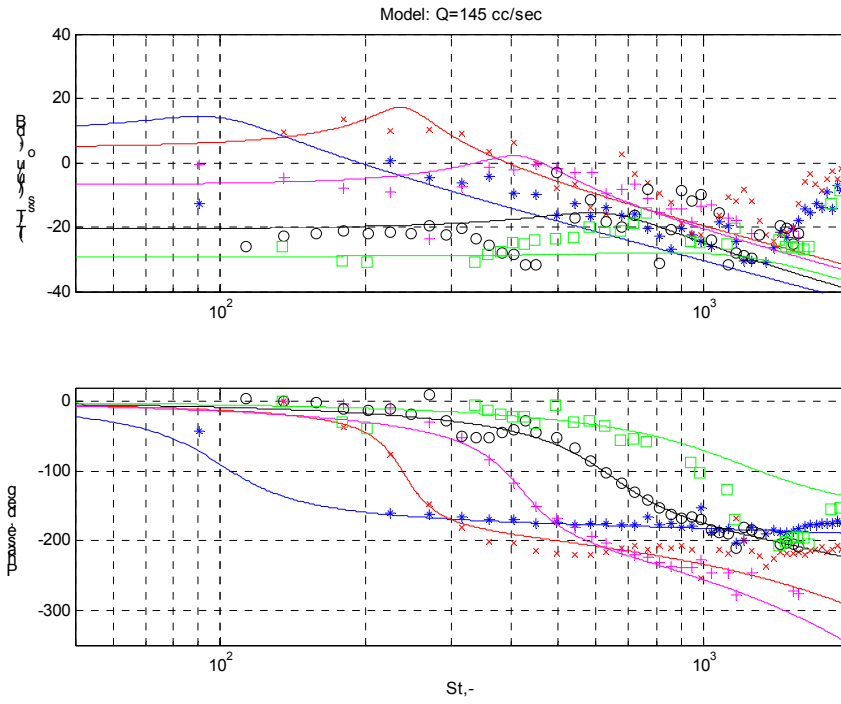


(a) natural frequency

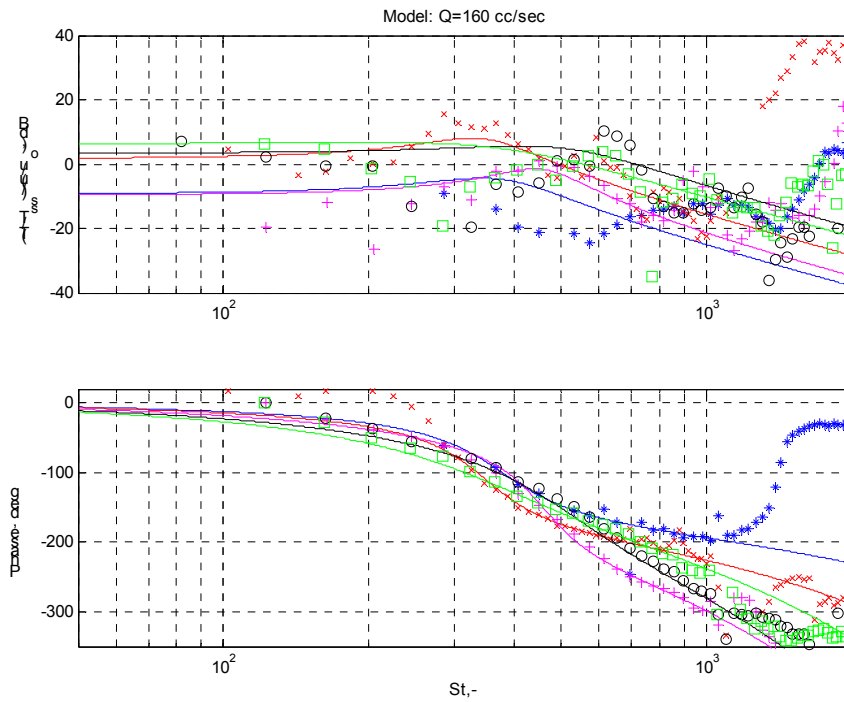


(b) damping ratio

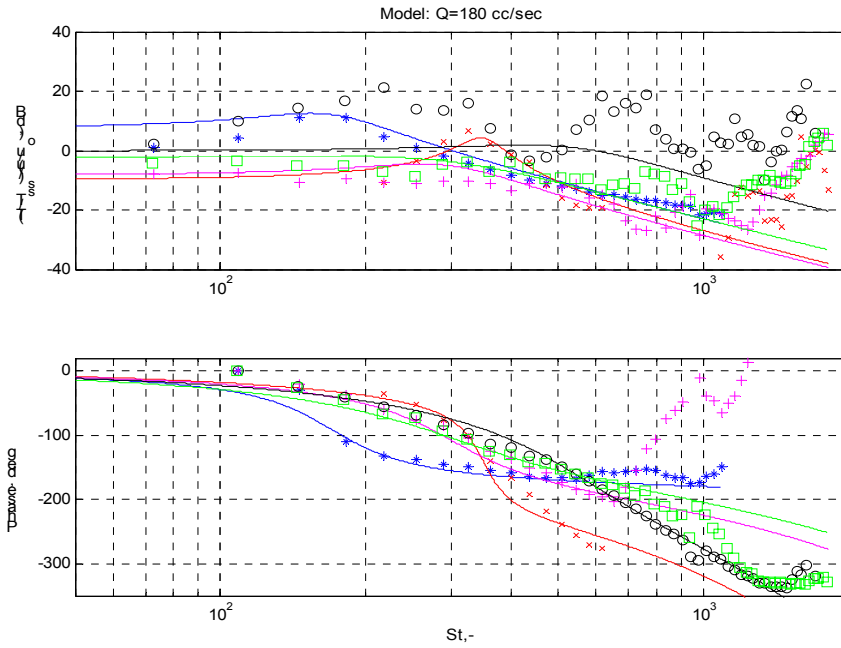
Figure 4.30. Parameters of the Dynamic Models of the Acoustic Forcing Function.
 Flow rates [cc/sec]: ○ 145, △ 160, □ 180, ◇ 200



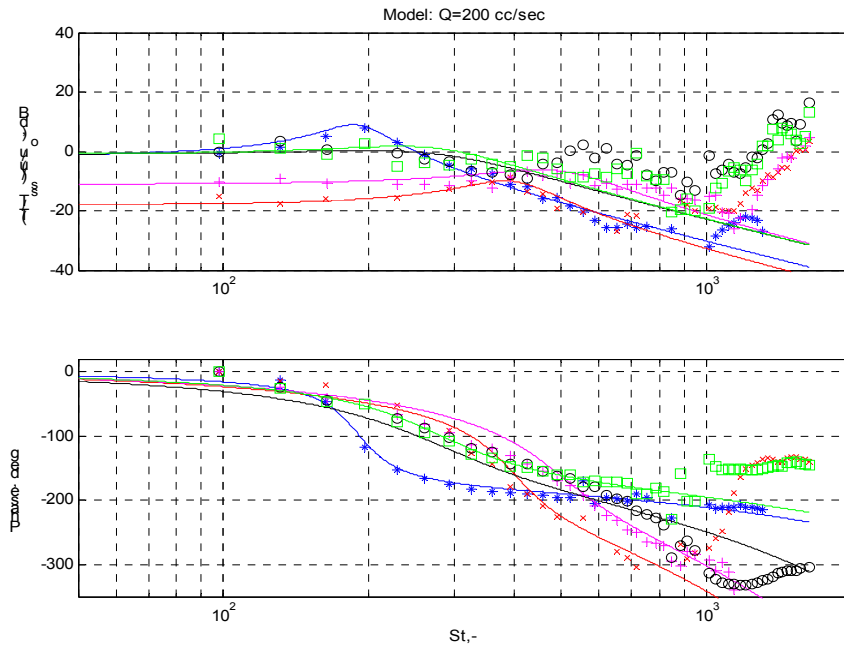
(a) Q=145 cc/sec



(b) Q=160 cc/sec

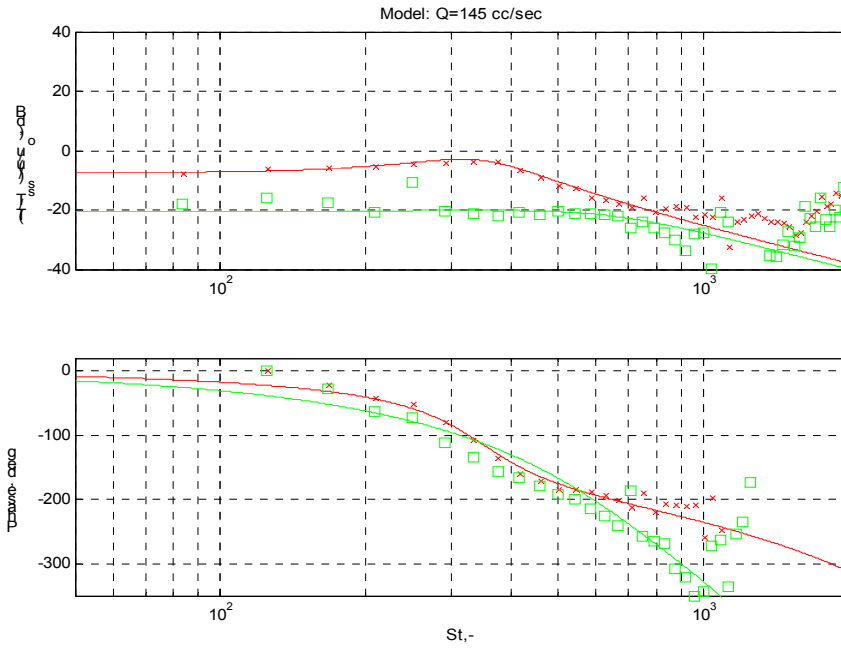


(c) Q=180 cc/sec

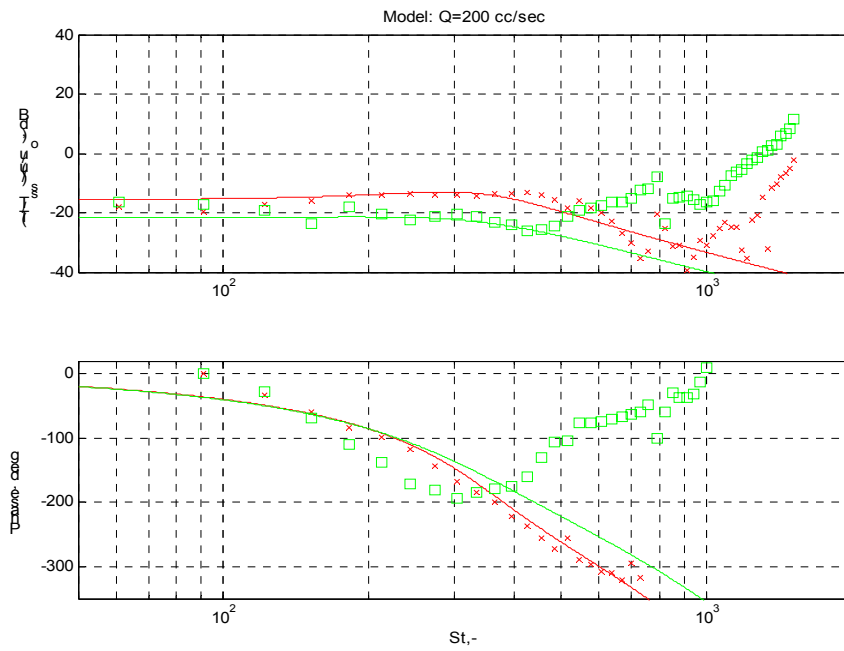


(c) Q=200 cc/sec

Figure 4.31. Dynamic Models of Acoustic Forcing Function Dynamics for Methane. Transfer functions were fit to the data plotted as a function of equivalence ratio * 0.50, x 0.55, + 0.60, o 0.65, □ 0.75.

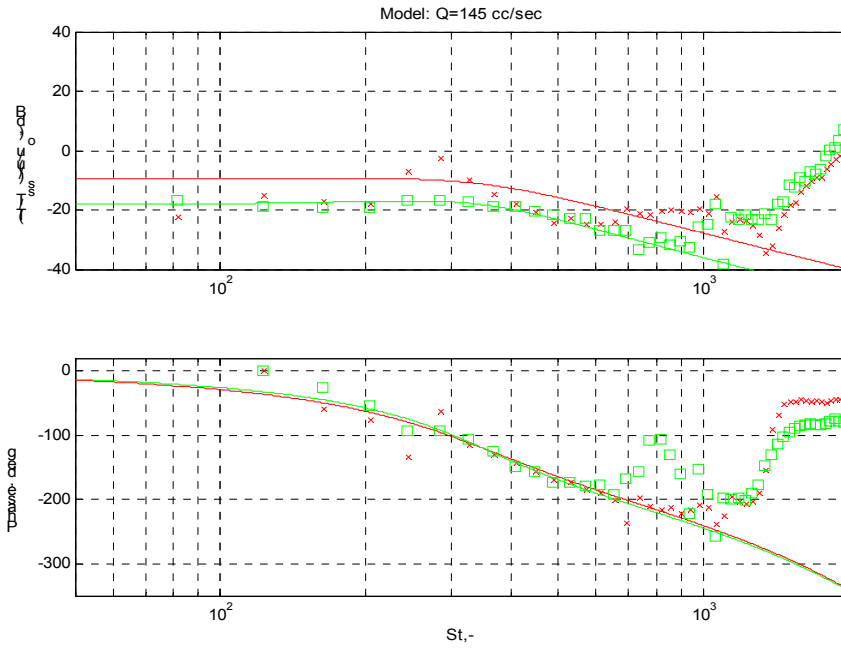


(a) $Q=145$ cc/sec

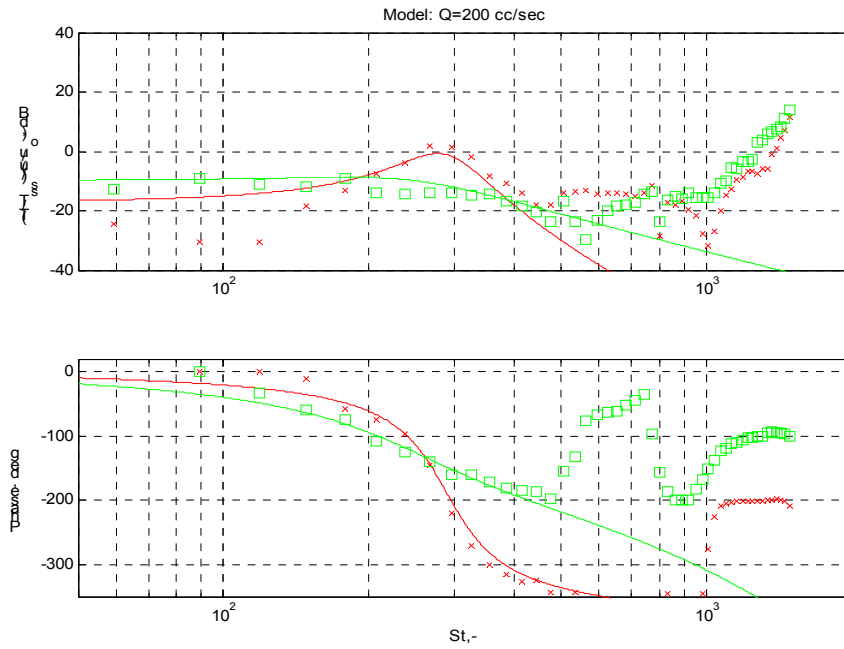


(b) $Q=200$ cc/sec

Figure 4.32. Dynamic Models of Acoustic Forcing Function Dynamics for Ethane. Transfer functions were fit to the data plotted as a function of equivalence ratio: \times 0.55, \square 0.75.



(a) Q=145 cc/sec



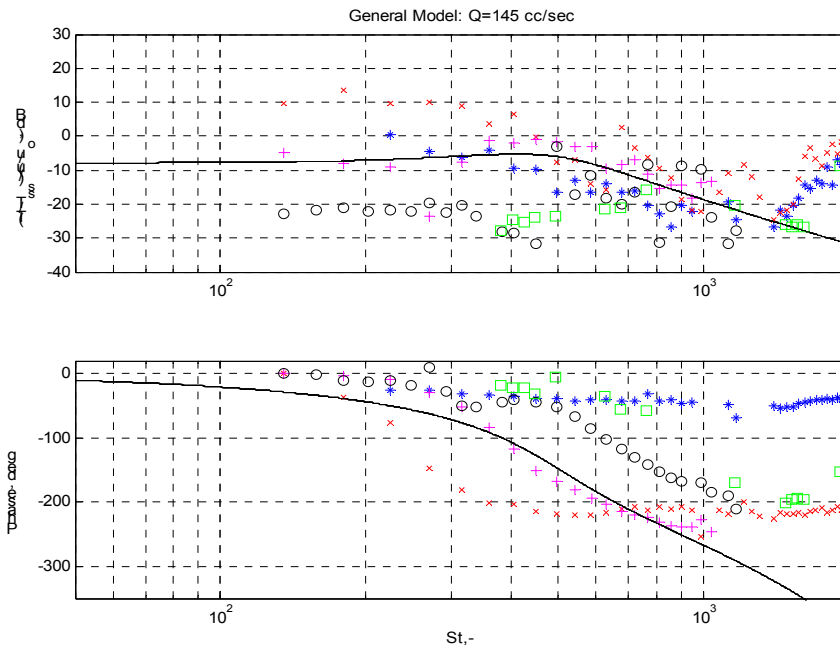
(b) Q=200 cc/sec

Figure 4.33. Dynamic Models of Acoustic Forcing Function Dynamics for Propane. Transfer functions were fit to the data plotted as a function of equivalence ratio: \times 0.55, \square 0.75.

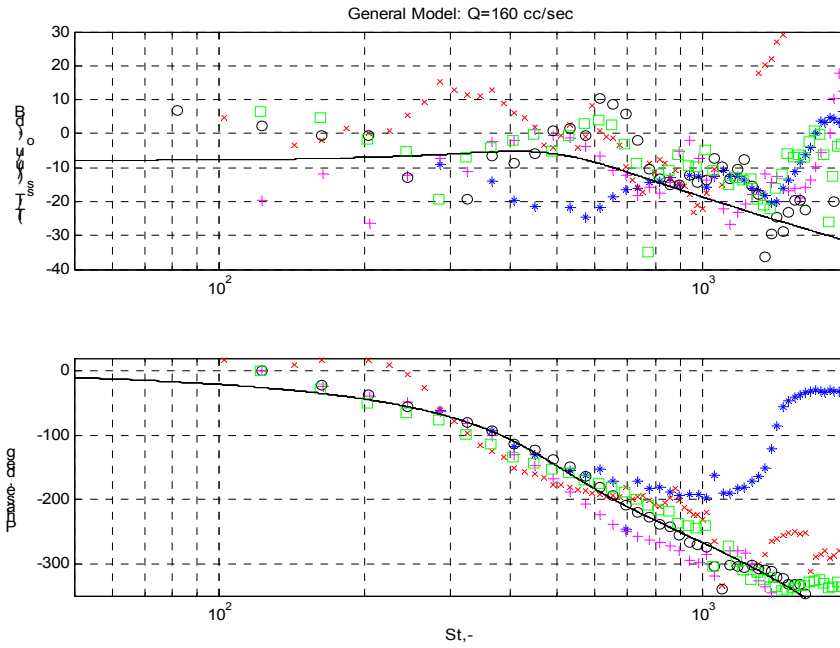
4.4.4 General Model. The dimensional analysis produced parameters by which the data could be presented in a more compact form. Many of the case models exhibit similar dynamic characteristics when put in dimensionless form. It was observed that a large portion of the data could be described through one general model. The form of the general model is the same as for the case models, shown by equation 4.9. The parameters for the generalized model are shown in Table 4.34. The data is plotted against the general model in Figures 4.35, 4.36, and 4.37 for methane, ethane, and propane. The lowest equivalence ratio and flow rate cases were the most likely to diverge from the model.

Table 4.34. General Model Parameters. The general model describes a large portion of the data well.

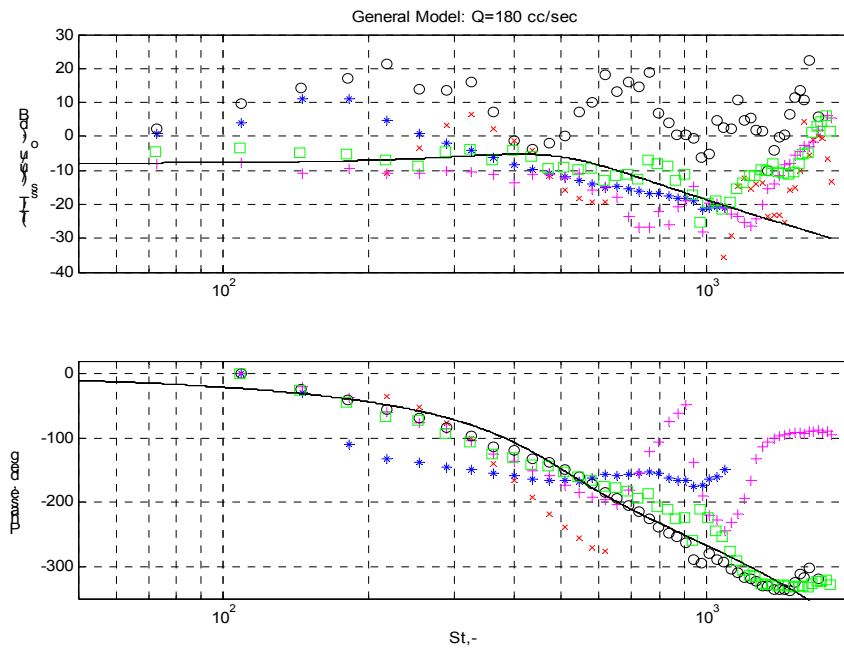
K	Tau	wn*	Z
1.00E+05	2.00E-03	500	0.40



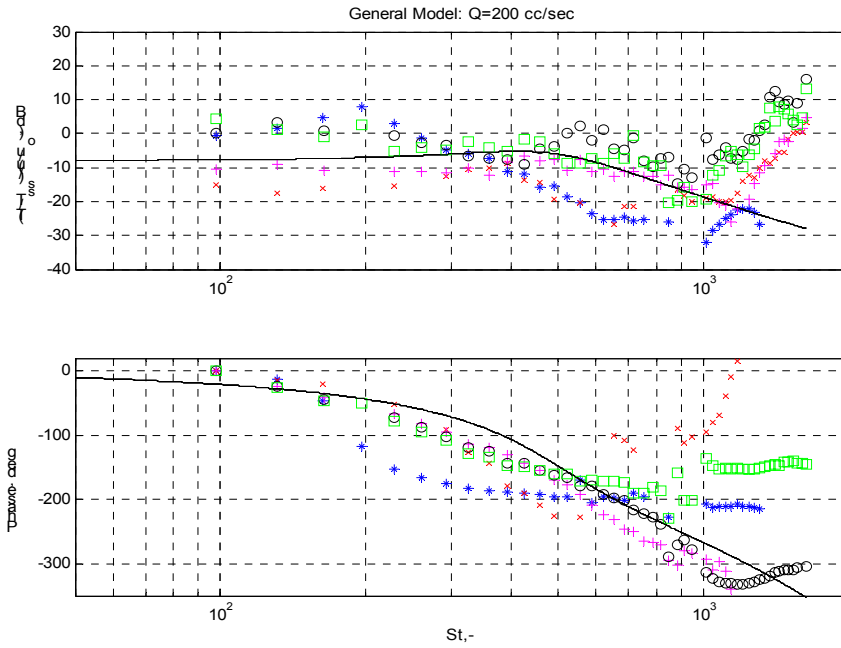
(a) Q=145 cc/sec



(b) Q=160 cc/sec

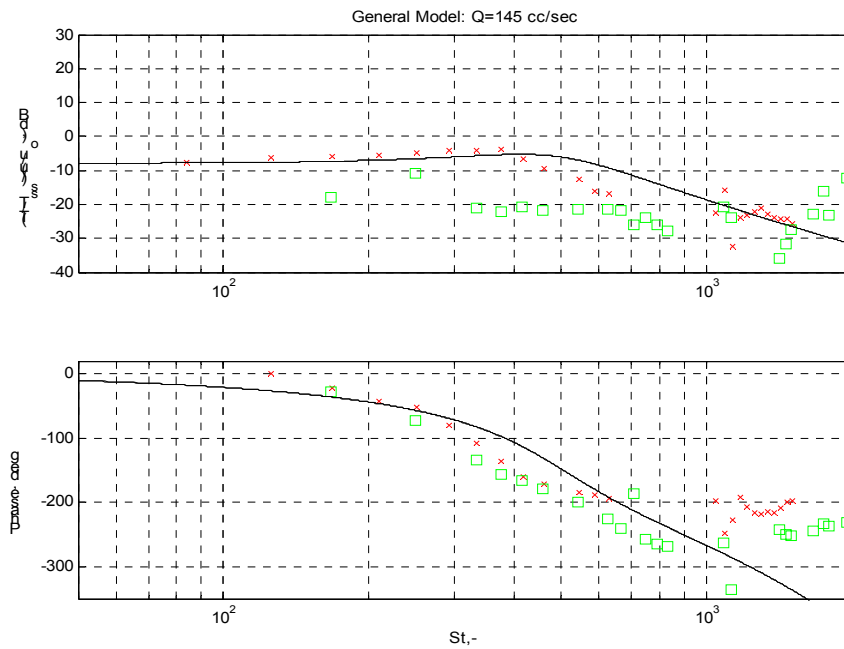


(c) Q=180 cc/sec



(d) $Q=200$ cc/sec

Figure 4.35. General Dynamic Model of Acoustic Forcing Function Dynamics for Methane. The general model describes the majority of the cases. Plotted as a function of equivalence ratio * 0.50, x 0.55, + 0.60, o 0.65, □ 0.75.



(a) $Q=145$ cc/sec

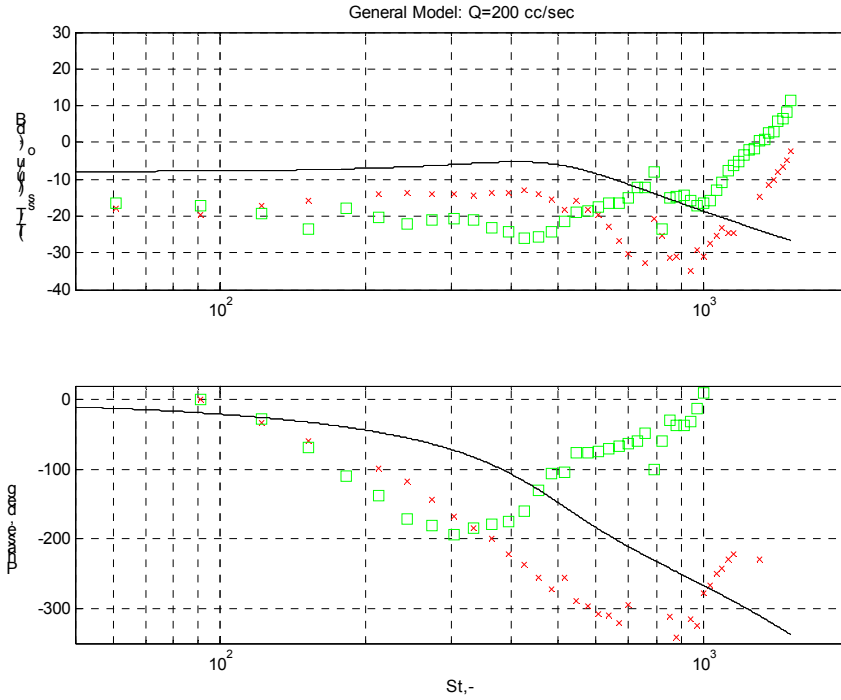
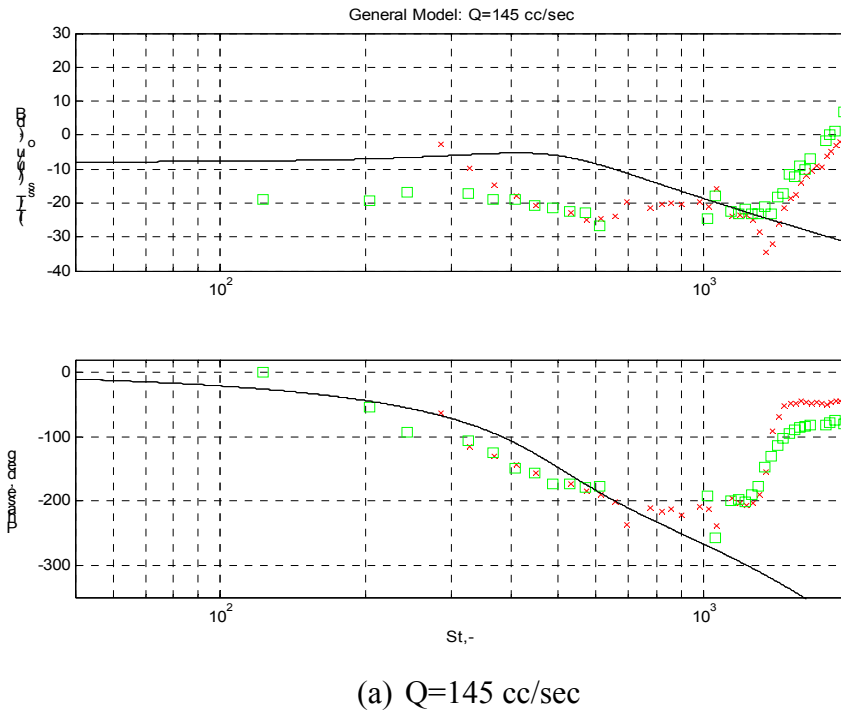
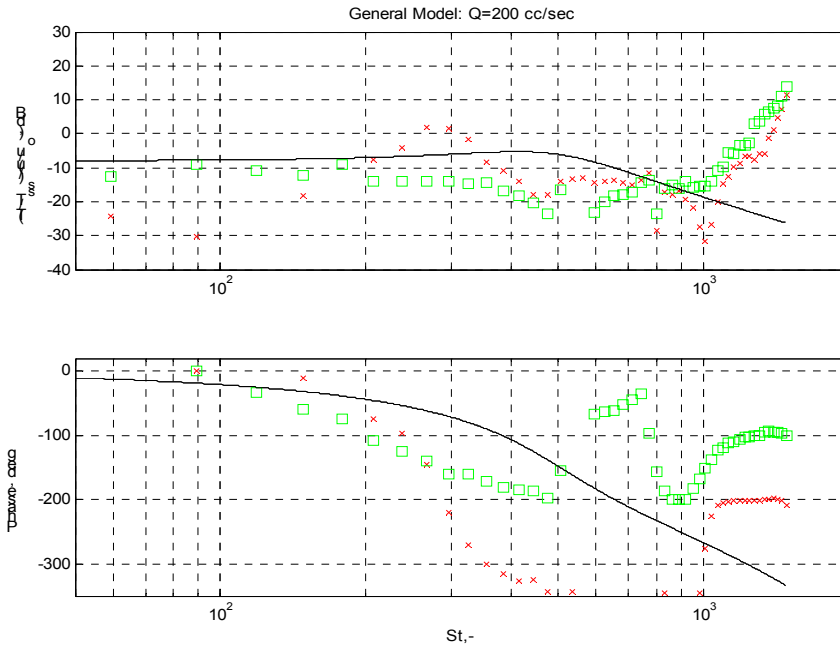


Figure 4.36. General Dynamic Model of Acoustic Forcing Function Dynamics for Ethane. The general model describes the majority of the cases. Plotted as a function of equivalence ratio: x 0.55, □ 0.75.





(b) $Q=200$ cc/se

Figure 4.37. General Dynamic Model of Acoustic Forcing Function Dynamics for Propane. The general model describes the majority of the cases. Plotted as a function of equivalence ratio: \times 0.55, \square 0.75.

4.5 Summary and Conclusions

The laminar flame dynamics study was completed to provide a baseboard for investigating turbulent flame dynamics. A methodology was formed of measuring open-loop frequency responses of flames and generating empirical dynamic models.

The laminar frequency response data yielded many interesting observations. As theorized, the dynamic behavior of OH^* chemiluminescence and product gas temperature differ significantly. This observation clarifies the importance of using diagnostics that measure the acoustic forcing function to determine flame transfer functions. The line-of-sight nature of the TDLAS measurement caused challenges in interpreting the frequency response functions, as 2-D phenomena were observed. The effect of different fuels on the dynamic characteristics of flames was also observed. Bandwidth is dependent on the

flame speed, while dynamic gain is reliant on the heat of formation. This topic holds great importance as biofuels and synthetic fuels gain popularity.

Through dimensional analysis, the dominant parameters affecting laminar flame dynamics were identified. When plotted in dimensionless form using Strouhal number as the abscissa, the data becomes more compact. Dynamic models, or flame transfer functions, were fit to the data. The models consist of two poles and time delay. Models indicate increasing resonant frequency and damping with increasing flow rate and equivalence ratio. A general model was proposed that describes the majority of the data. Aberrations from the general model may be due to incorrect calculation of the flame speed and interpretation of the TDLAS data.

The laminar flame dynamics study allowed a detailed look at flame dynamics in a simple system. The physical parameters relevant to laminar flame dynamics were ascertained. The methodologies developed can now be applied to more complex combustion systems.

Bibliography

1. Haber, L. and U. Vandsburger. *Combustion and heat transfer dynamics in a premixed laminar flat-flame burner*. in *Aerospace Sciences Meeting*. 2004.
2. Simons, T.D., R.H. Eustis, and M. Mitchner. *Measurements of propagating acoustic and entropy waves in a combustion MHD generator*. in *Engineering aspects of magnetohydrodynamics*. 1982. University of California, Irvine.
3. Markstein, G.H., *Nonsteady Flame Propagation*. 1964, Oxford, England: Pergamon Press.
4. Baillot, E., D. Durox, and R. Prud'homme, *Experimental and theoretical study of a premixed vibrating flame*. *Combustion & Flame*, 1992. **88**: p. 149-168.
5. Batley, G.A., et al., *A numerical study of the vorticity field generated by the baroclinic effect due to the propagation of a planar pressure wave through a cylindrical premixed laminar flame*. *Journal of Fluid Mechanics*, 1994. **279**: p. 217-237.
6. Lee, D. and T. Lieuwen. *Acoustic nearfield characteristics of a premixed flame in a longitudinal acoustic field*. in *Proceedings of ASME Turbo Expo*. 2001.
7. Lieuwen, T., *Theoretical investigation of unsteady flow interactions with a premix planar flame*. *Journal of Fluid Mechanics*, 2001. **435**: p. 289-303.

8. Kee, R., et al., *A fortran program for modeling steady laminar one-dimensional flames*. 1993, Sandia National Laboratories.
9. Smith, P., et al., http://www.me.berkeley.edu/gri_mech/. 1999.
10. Turns, S., *An introduction to combustion*. 2 ed. 1999: McGraw-Hill Science/Engineering/Math.
11. Kuo, K.K., *Principles of Combustion*. 1986: Interscience.
12. McIntosh, A.C. and S. Rylands, *A model of heat transfer in Rijke tube burners*. *Combustion Science and Technology*, 1996. **113-114**: p. 273-289.
13. Szucs, E., *Similitude and Modeling*. 1979: Elsevier Science Ltd.
14. Schuller, T., D. Durox, and S. Candel, *A unified model for the prediction of laminar flame transfer functions: comparisons between conical and V-flame dynamics*. *Combustion & Flame*, 2003. **134**: p. 21-34.